

# Manganese Coordination Micelles That Activate Stimulator of Interferon Genes and Capture In Situ Tumor Antigens for Cancer Metalloimmunotherapy

Jiexin Li, He Ren, Qian Qiu, Xingyue Yang, Jingyu Zhang, Chen Zhang, Boyang Sun, Jonathan F. Lovell, and Yumiao Zhang\*



Cite This: *ACS Nano* 2022, 16, 16909–16923



Read Online

ACCESS |

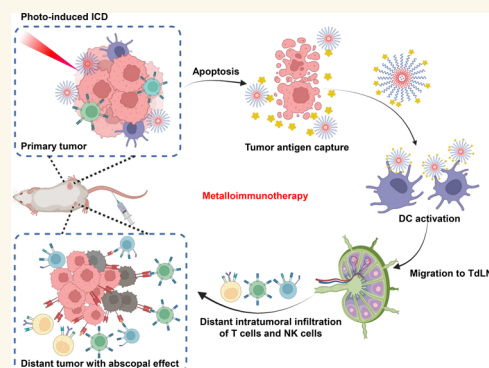
Metrics & More

Article Recommendations

Supporting Information

**ABSTRACT:** Cancer immunotherapy holds great promise but is generally limited by insufficient induction of anticancer immune responses. Here, a metal micellar nanovaccine is developed by the self-assembly of manganese (Mn), a stimulator of interferon genes (STING) agonist (ABZI) and naphthalocyanine (ONc) coordinated nanoparticles (ONc-Mn-A) in malimide-modified Pluronic F127 (malF127) micelles. Owing to synergy between Mn and ABZI, the nanovaccine, termed ONc-Mn-A-malF127, elevates levels of interferon- $\beta$  (IFN $\beta$ ) by 324- and 8-fold in vivo, compared to use of Mn or ABZI alone. As such, the activation of the cyclic guanosine monophosphate-adenosine monophosphate synthase (cGAS)-STING pathway induces sufficient dendritic cell (DC) maturation, eventually resulting in the death of CD8<sup>+</sup> T cell-sensitive tumors and CD8<sup>+</sup> T cell-resistant tumors by simultaneously promoting cytotoxic CD8<sup>+</sup> T cells and NK cells, respectively. Furthermore, with ONc used as a Mn chelator and an efficient photosensitizer, photoinduced immunogenic cell death (ICD) of tumor cells releases damage-associated molecular patterns (DAMPs) and neoantigens from dying primary tumor cells upon laser irradiation, which are captured in situ by malF127 in tumor cells and then transported to DCs. After laser treatment, in addition to the photothermal therapy, immune responses characterized by the level of IFN $\beta$  are further elevated by another 4-fold. In murine cancer models, ICD-based metalloimmunotherapy using the ONc-Mn-A-malF127 nanovaccine in a single dose by intravenous injection achieved eradication of primary and distant tumors. Taken together, ONc-Mn-A-malF127 offers a nanoplatform to enhance anticancer efficacy by metalloimmunotherapy and photoinduced ICD based immunotherapy with strong abscopal effect.

**KEYWORDS:** metalloimmunotherapy, cGAS-STING pathway, abscopal effect, immunogenic cell death, IFN $\beta$  enhanceosome



## INTRODUCTION

Immunotherapy has emerged as a powerful strategy for cancer treatment.<sup>1</sup> However, only about 20% of cancer patients respond to immunotherapy,<sup>2–4</sup> which could be ascribed to insufficient cytotoxic CD8<sup>+</sup> T cells and to tumors also being able to evade CD8<sup>+</sup> T cells through selective loss of major histocompatibility complex (MHC) class I expression.<sup>5,6</sup> It has been shown that activation of cytotoxic natural killer (NK) cells could not only directly kill tumors that evade T cell responses but also enhance the adaptive antitumor immune response.<sup>7–9</sup> However, both cytotoxic CD8<sup>+</sup> T cells and NK cells are required to be activated for potent immune responses.

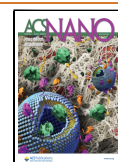
Activation of the cyclic guanosine monophosphate-adenosine monophosphate synthase–stimulator of interferon genes

(cGAS-STING) pathway has attracted research interest owing to its important role in the antitumor response of CD8<sup>+</sup> T cell-sensitive and CD8<sup>+</sup> T cell-resistant tumors.<sup>7,10</sup> Once the cGAS enzyme binds to double-stranded DNA catalyzing formation of 2',3'-cyclic guanosine monophosphate–adenosine monophosphate (cGAMP), the STING protein could be ultimately activated. The activated STING can act as a second messenger

Received: July 13, 2022

Accepted: September 30, 2022

Published: October 6, 2022



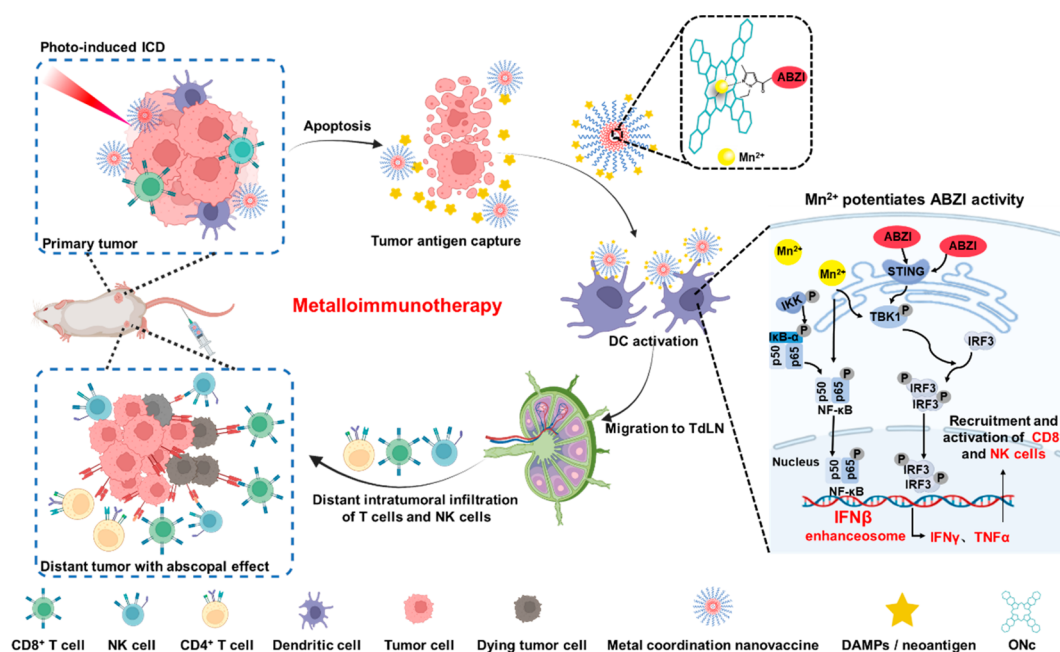


**Figure 1.** Schematic illustration of manganese coordination micelles for PTT-mediated ICD effect, tumor antigen capture, and enhanced activation of the cGAS-STING pathway to eradicate primary and distant tumors.

that activates the cGAS-STING pathway and promotes the production of type I interferon (IFN).<sup>11</sup> The large amount of type I interferon produced not only can enhance the activation of CD8<sup>+</sup> T cells by upregulating co-stimulatory molecules (CD40, CD86, etc.)<sup>12,13</sup> but also can induce interleukin (IL)-15 and IL-15 receptor (IL15R $\alpha$ ) to enhance NK cell activity.<sup>7,14</sup> Clinical studies on STING agonists mainly involve the use of cyclic dinucleotides (CDNs) such as 2',3'-cyclic [G(2',5')pA(3',5')p] and cyclic di-AMP.<sup>15,16</sup> However, free CDNs are easily degraded by ecto-nucleotide pyrophosphatase/phosphodiesterase present in human or murine serum.<sup>17</sup> Free CDNs cannot easily permeate through membranes and may trigger adverse reactions such as induction of T cell apoptosis.<sup>18,19</sup> Amidobenzimidazole-based STING agonists such as ABZI and di-ABZI generally have lower EC<sub>50</sub> values, indicative of higher ability of stimulating STING. For example, EC<sub>50</sub>(2',3'-cyclic [G(2',5')pA(3',5')p]) is about 87.55  $\mu\text{mol L}^{-1}$ , whereas EC<sub>50</sub> of ABZI is only 0.49  $\mu\text{mol L}^{-1}$ .<sup>20,21</sup>

Manganese (Mn) is a nutritional inorganic trace element required for a variety of important physiological processes such as neuronal functions and antioxidant defenses.<sup>22,23</sup> Mn (Mn<sup>2+</sup> in general cases) incorporates into a number of metalloenzymes such as Mn superoxide dismutase (SOD, Mn<sup>3+</sup> or Mn<sup>2+</sup> in this case), arginase, pyruvate carboxylase, and glutamine synthetase,<sup>24</sup> where it plays a critical cofactor role in the functions of these enzymes. In addition, Mn<sup>2+</sup> is also an essential adjuvant for the regulation of innate immune sensing of tumors. Mice deficient in Mn have reduced tumor-infiltrating CD8<sup>+</sup> T cells, leading to significant tumor growth and metastasis.<sup>25</sup> Mn<sup>2+</sup> can activate cGAS-STING signaling by inducing phosphorylation of TBK1 and p65; therefore, it can enhance STING agonist activity by generation of IFN $\beta$  enhanceosomes.<sup>25–28</sup> Manganese-based nanomaterials such as manganese phosphate nanoclusters,<sup>29</sup> CDN–Mn<sup>2+</sup> particles,<sup>26</sup> and manganese nanoadjuvant (MnARK)<sup>30</sup> have been developed to activate the STING pathway of dendritic cells in tumor sites. However, the efficacy is still not satisfactory, or

multiple vaccinations are required. One of the possible reasons is that in the tumor microenvironment, cancer cells significantly outnumber the tumor-infiltrating dendritic cells in the tumor site, leading to insufficient uptake of vaccines in dendritic cells and severely attenuated STING activation.<sup>31,32</sup>

Immunogenic cell death (ICD) induced by radiation therapy or photothermal therapy releases high mobility group B1 (HMGB1) and tumor-derived protein antigens (TDPAs).<sup>33,34</sup> HMGB1 can act as a “find me” signal to recruit more dendritic cells (DCs) in tumor sites. The enhanced phagocytosis of tumor antigens by DCs gives rise to activation of T cells to induce a tumor-specific antitumor immune response.<sup>33,35</sup> Due to the inherent immune clearance in the body, the released TDPAs will be rapidly cleared, resulting in ineffective activation of antitumor immune response and the inability to induce abscopal effect. Therefore, nanocarriers with antigen capture features have been developed by chemically grafting protein capture groups such as amino,<sup>36</sup> catechol,<sup>37</sup> and maleimide<sup>36,38</sup> moieties. Consequently, the retention time of antigens in tumor sites could be prolonged and tumor antigens could be ferried to DCs in the nanoparticle form, triggering a strong immune response.

Here, we propose a strategy based on PTT-mediated ICD effect and synergistically enhanced activation of the cGAS-STING pathway by dual adjuvants (Figure 1). A Mn-ONc-A-malF127 coordinated nanovaccine was developed, and the mechanism of the metal vaccine is based on the exceptionally synergized adjuvant effect of ABZI and Mn. After a single systemic administration, the photosensitizer naphthalocyanine (ONc) can induce ICD to kill a primary tumor under laser irradiation, resulting in the release of TDPAs and recruitment of DCs. The maleimide-modified F127 (malF127) can effectively capture TDPAs, and the as-formed nanovaccine in situ can co-deliver adjuvant and antigen to DCs. The cGAS-STING pathway of DCs phagocytosing antigen@ONc-Mn-A-malF127 was activated by Mn<sup>2+</sup> and the STING agonist ABZI. As a bridge of innate and adaptive antitumor immunity, the

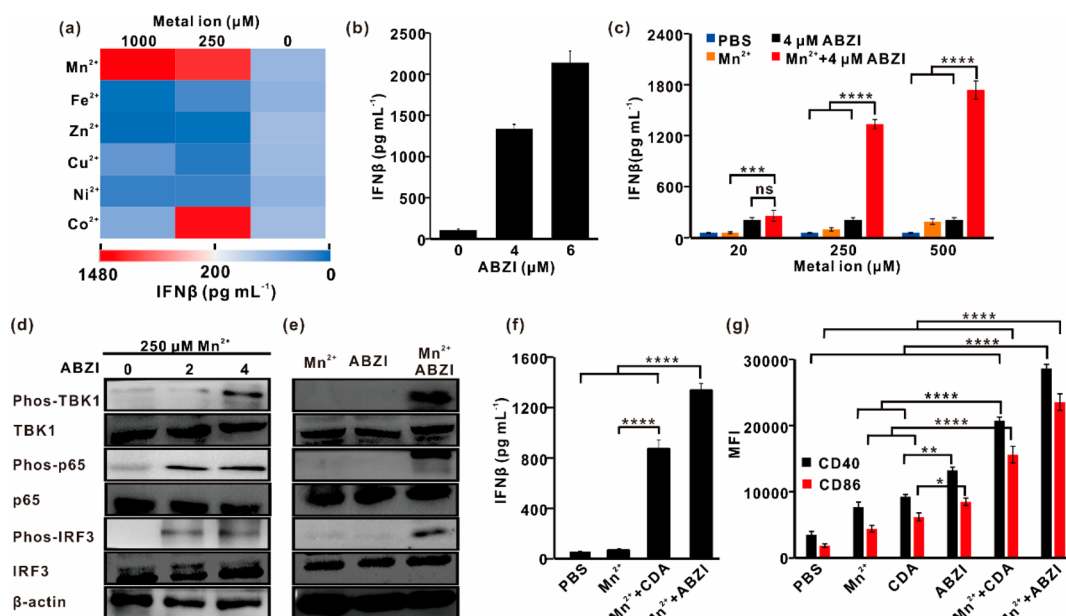


**Figure 2.** Combination of  $\text{Mn}^{2+}$  and STING agonist ABZI promotes the cGAS/STING signaling transduction. (a)  $\text{IFN}\beta$  secretion was quantified after BMDCs were incubated with various concentrations of metal ions with  $4 \mu\text{M}$  ABZI for 24 h. (b)  $\text{IFN}\beta$  secretion was quantified after BMDCs were incubated with various concentrations of ABZI with  $250 \mu\text{M}$  metal ions for 24 h. (c) BMDCs were treated with various concentrations of  $\text{Mn}^{2+}$  with  $4 \mu\text{M}$  ABZI, and after 24 h mouse  $\text{IFN}\beta$  secretion was quantified by ELISA. Western blot analysis of the activation of the cGAS-STING-IFN-I pathway in BMDCs after treatment with (d) increasing concentrations of ABZI with  $250 \mu\text{M}$   $\text{Mn}^{2+}$  or (e)  $4 \mu\text{M}$  ABZI and  $250 \mu\text{M}$   $\text{Mn}^{2+}$  for 6 h; representative data from two independent experiments with similar results are shown. TBK1, p65, IRF3, and  $\beta$ -actin were used as the loading control. (f) Comparison of  $\text{IFN}\beta$  secretion quantified by ELISA after BMDCs were treated with PBS,  $250 \mu\text{M}$   $\text{Mn}^{2+}$ ,  $250 \mu\text{M}$   $\text{Mn}^{2+}$  +  $4 \mu\text{M}$  CDA, or  $250 \mu\text{M}$   $\text{Mn}^{2+}$  +  $4 \mu\text{M}$  ABZI. (g) Quantification of CD40 and CD86 biomarkers by flow cytometry indicating BMDC maturation after BMDCs were treated with various formulations for 24 h. MFI indicates mean fluorescence intensity. Statistical significance was calculated via one-way ANOVA with Tukey's test: \* $p < 0.05$ ; \*\* $p < 0.01$ ; \*\*\* $p < 0.001$ ; \*\*\*\* $p < 0.0001$ .

nanosystem can combine the action of both  $\text{CD8}^+$  T cells and NK cells to kill  $\text{CD8}^+$  T cell-sensitive and -resistant tumors, completely eradicating primary and distant tumors.

## RESULTS AND DISCUSSION

**$\text{Mn}^{2+}$  Enhances cGAS-STING Pathway Activation by STING Agonist.** In order to enhance the activation of the cGAS-STING pathway in immune cells, we synthesized a STING agonist ABZI derivative (Figures S1–21, Table S1, Supporting Information) and investigated the activation and amplification of the cGAS-STING-IFN-I pathway by different metal ions, including  $\text{Mn}^{2+}$ ,  $\text{Fe}^{2+}$ ,  $\text{Zn}^{2+}$ ,  $\text{Cu}^{2+}$ ,  $\text{Ni}^{2+}$ , and  $\text{Co}^{2+}$ , in combination with STING agonist ABZI derivatives. Surprisingly, the addition of  $\text{Mn}^{2+}$  or  $\text{Co}^{2+}$  significantly enhanced type I IFN production in bone marrow-derived dendritic cells (BMDCs) compared to ABZI alone (Figure 2a). Given that the best adjuvant property was from  $\text{Mn}^{2+}$ , which was also previously shown to effectively activate the cGAS-STING pathway to enhance innate immunity,<sup>32,39</sup> we chose  $\text{Mn}^{2+}$  to investigate the interaction of metal and ABZI for further studies. With the increase in  $\text{Mn}^{2+}$  or ABZI concentrations, the STING pathway in BMDCs was more efficiently activated, as indicated by increasing type I IFN production (Figure 2b,c). cGAS-STING pathway activation is mainly regulated by the phosphorylation of tank-binding kinase 1 (TBK1), p65, and interferon regulatory factor 3 (IRF3), resulting in the release of type I interferon.<sup>40,41</sup> Therefore, to investigate the mechanism by which  $\text{Mn}^{2+}$  enhances the activity of the STING agonist ABZI, we analyzed the secretion levels of phosphorylated p65, TBK1, and IRF3 to evaluate the downstream STING pathway by Western blotting (Figure 2d,e). As expected, the

concentration of phosphorylated p65, TBK1, and IRF3 in BMDCs was significantly increased after the addition of  $\text{Mn}^{2+}$ , compared with ABZI alone (Figure 2d,e). Thus, these data show that  $\text{Mn}^{2+}$  enhances the STING signal cascade and type I interferon production by p65, TBK1, and IRF3 phosphorylation in the cGAS-STING-IFN-I signal pathway by STING agonists. Moreover,  $\text{Mn}^{2+}$  + ABZI significantly up-regulated the expression of CD40 and CD86, which are biomarkers of BMDC maturation (Figure 2g). STING agonists currently used in clinical trials include nucleotide agonists such as 2',3'-cyclic [G(2',5')pA(3',5')p] and cyclic di-AMP (CDA).<sup>42</sup> Although recent evidence has revealed that  $\text{Mn}^{2+}$  can augment IFN-I activity of CDA,<sup>26</sup> we found that compared with the nucleotide STING agonists such as CDA, ABZI as an amidobenzimidazole-based STING agonist could induce more secretion of type I IFN and the up-regulation of BMDC maturation markers (CD40 and CD86) with synergistic enhancement by  $\text{Mn}^{2+}$  (Figure 2f,g). In addition to stronger activation of the cGAS-STING pathway to potentiate innate immunity using ABZI instead of CDA, nucleotide-based STING agonists are also prone to degradation by ecto-nucleotide pyrophosphatase/phosphodiesterase (ENPP1),<sup>43</sup> which abundantly exists in murine and human blood and also tumor microenvironments, resulting in impaired immune function for the treatment of tumors and other diseases.<sup>44,45</sup>

**Characterization of ONc-Mn-A-malF127 Nanomicelles and DC Maturation in Vitro.** Although free  $\text{Mn}^{2+}$  + ABZI can effectively activate innate immunity, the free form of the mixture has limitations compared to nanoparticles, such as poor systemic stability, low cellular uptake rate, inability to

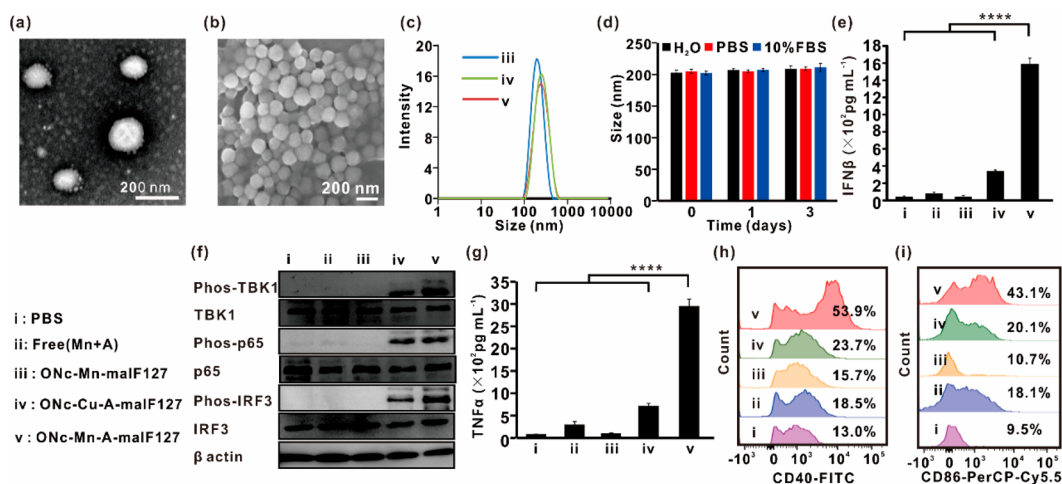


**Figure 3.** Characterization of ONc-Mn-A-malF127 nanoparticles. (a) Transmission electron microscope image of ONc-Mn-A-malF127. (b) Scanning electron microscope image of ONc-Mn-A-malF127. (c, d) Dynamic light scattering (c) and stability (d) of ONc-Mn-A-malF127. (e) BMDCs were treated for 24 h with 2  $\mu$ M ABZI and 15  $\mu$ M Mn<sup>2+</sup> in PBS or formulations ii–v followed by quantification of IFN $\beta$  secretion by enzyme-linked immunosorbent assay (ELISA). (f) Western blot analysis of the activation of the cGAS-STING-IFN-I pathway in BMDCs after treatment with different sample containing 2  $\mu$ M ABZI and 15  $\mu$ M Mn<sup>2+</sup> for 6 h; representative data from two independent experiments with similar results are shown: (i) PBS, (ii) free Mn + A, (iii) ONc-Mn-malF127, (iv) ONc-Cu-A-malF127, (v) ONc-Mn-A-malF127. TBK1, p65, IRF3, and  $\beta$ -actin were used as the loading control. (g) BMDCs were treated for 24 h with 2  $\mu$ M ABZI and 15  $\mu$ M Mn<sup>2+</sup> in PBS or formulations ii–v followed by quantification of TNF $\alpha$  secretion by enzyme-linked immunosorbent assay (ELISA). (h, i) BMDCs were treated for 24 h with 2  $\mu$ M ABZI and 15  $\mu$ M Mn<sup>2+</sup> in PBS or formulations ii–v, followed by analysis for CD40 (h) and CD86 (i) expression by flow cytometry. Statistical significance was calculated via one-way ANOVA with Tukey's test: \* $p$  < 0.05; \*\* $p$  < 0.01; \*\*\* $p$  < 0.001; \*\*\*\* $p$  < 0.0001.

achieve co-delivery of payloads, and potential safety concerns at large doses.<sup>46</sup> Therefore, we designed a delivery system that can co-deliver Mn<sup>2+</sup>, STING agonist ABZI, and photosensitizer 5,9,14,18,23,27,32,36-octabutoxy-2,3-naphthalocyanine (ONc) that can activate a potent innate immune response with reduced dose (Figure 1). Based on the coordination interaction of metal ions in the center of ONc or with imidazole-like structure containing ABZI, Mn<sup>2+</sup>, ABZI, and ONc could self-assemble into nanoparticles (ONc-Mn-A) in tetrahydrofuran solution. In order to improve the stability and water solubility of ONc-Mn-A nanoparticles, we encapsulated the hydrophobic ONc-Mn-A nanoparticles in the hydrophobic core of maleimide-modified Pluronic F127 (malF127) to form stable nanomicelles, termed ONc-Mn-A-malF127 nanomicelles. The addition of Mn resulted in obvious red shift of the ONc absorption spectrum, and the fluorescence of ABZI could be used for quantification (Figure S23). The chelation of ONc made the whole nanomicelle more stable, because Mn<sup>2+</sup>–ABZI could not be effectively encapsulated in F127 to form stable micelles (Figure S23). The resulting ONc-Mn-A-malF127 nanomicelles exhibited a homogeneous spherical shape with an average hydrodynamic diameter of 180 nm  $\pm$  15 nm (Figure 3a–c) and exhibited good stability in H<sub>2</sub>O, PBS, and 10% FBS within 3 days (Figure 3d).

In order to demonstrate that Mn<sup>2+</sup> enhances STING agonist activity and induces the maturation of DCs, we prepared an admixture of free ABZI and Mn<sup>2+</sup> (formulation ii), malF127 micelles encapsulating ONc and Mn without ABZI (ONc-Mn-malF127, formulation iii), malF127 micelles encapsulating ONc-Cu-ABZI as a control to show the effect of Mn (ONc-Cu-A-malF127, formulation iv), and malF127 micelles encapsulating ONc-Mn-ABZI (ONc-Mn-A-malF127, formulation v). ONc-Mn-A-malF127 nanomicelles significantly increased the secretion of IFN $\beta$  in BMDCs, >12 times higher than controls (Figure 3e), which was ascribed to STING-

dependent p65, TBK1, and IRF3 phosphorylation to activate the cGAS-STING pathway (Figure 3f). For tumor necrosis factor alpha (TNF $\alpha$ ), ONc-Mn-A-malF127 nanomicelles also produced a similar effect, inducing >5 times higher response than controls (Figure 3g). Most importantly, the large amount of type I interferons produced has been demonstrated before to upregulate co-stimulatory molecule expression to activate DCs.<sup>47,48</sup> Obviously, the ONc-Mn-A-malF127 nanomicelles are capable of co-delivering Mn<sup>2+</sup> and ABZI to significantly increase the expression of CD40 and CD86 co-stimulatory molecules, subsequently inducing the maturation of DCs and enhanced antigen-presenting ability (Figure 3h,i). Enhanced DC maturation can prime T cells to activate CD8<sup>+</sup> T cells for enhanced antitumor immunity.<sup>47</sup>

**In Vivo Assessment of ONc-Mn-A-malF127 for Metalloimmunotherapy.** Although direct intratumoral injection is used for safety reasons and also due to the poor stability of STING agonists, this route is generally not effective for metastatic disease.<sup>49</sup> The nanomicelles designed in this study have good stability in blood (Figure 3d). Therefore, we next investigated the therapeutic effect of ONc-Mn-A-malF127 nanomicelles in vivo after systemic administration. CT26 tumor-bearing 6–8 week-old BALB/c mice were injected intravenously with PBS, free Mn<sup>2+</sup> + ABZI, ONc-Mn-malF127 nanomicelles, ONc-Cu-A-malF127 nanomicelles, or ONc-Mn-A-malF127 nanomicelles on days 0 and 5 (Figure 4a). Compared with other controls, intravenous injection of ONc-Mn-A-malF127 resulted in enhanced immune activation, characterized by the significant increase of IFN $\beta$ , TNF $\alpha$ , and CXCL10 in serum (Figure 4b), which demonstrated that Mn<sup>2+</sup> and ABZI sensitized the cGAS-STING pathway in vivo. Abundant production of the chemokine CXCL10 recruits adoptively transferred CXCR3<sup>+</sup> effector CD8<sup>+</sup> T cells to clear tumors.<sup>50</sup> The stable body weight of mice demonstrated that there was no noticeable systemic toxicity after systemic

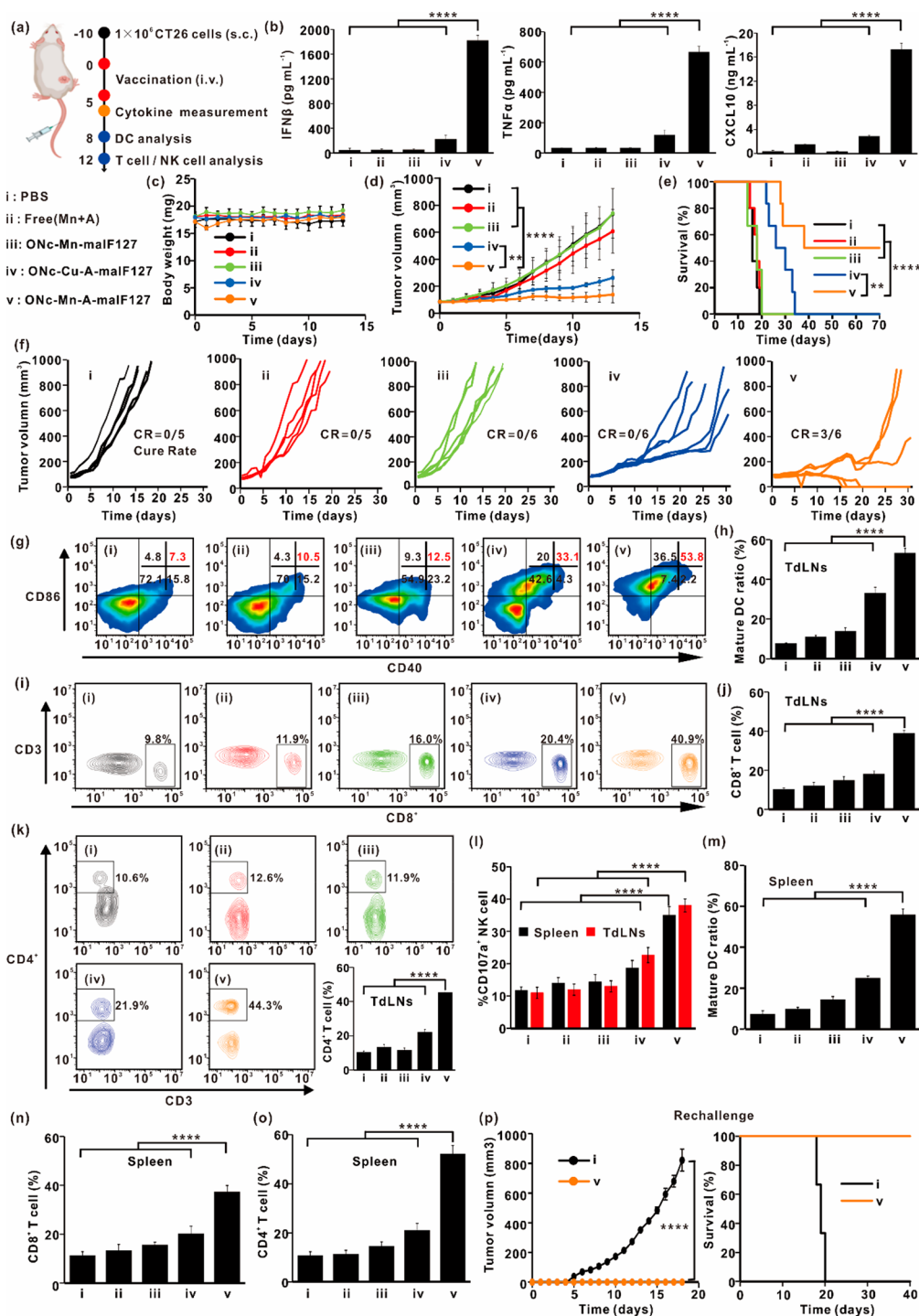


**Figure 4.** In vivo metalloimmunotherapy by intravenous injection of ONc-Mn-A-malF127 on CT26 tumors after iv administration: CT26 tumor-bearing BALB/c mice were treated intravenously with various samples, containing 10  $\mu\text{g}$  of ABZI, 10  $\mu\text{g}$  of Mn<sup>2+</sup>, and 50  $\mu\text{g}$  of ONc, on days 0 and 5 (a); serum cytokines were measured by ELISA 6 h after the second dose (b): (i) PBS, (ii) free Mn<sup>2+</sup> + ABZI, (iii) ONc-Mn-malF127, (iv) ONc-Cu-A-malF127, (v) ONc-Mn-A-malF127. (c) Body weight of mice during various treatments. (d–f) Animal survival (d, e) and tumor growth (f) were monitored every day. Statistical significance of tumor growth and survival rate was calculated via two-way ANOVA with Tukey's test and log-rank test, respectively. (g, h) Representative flow cytometry plots (g) and quantification of mature DCs (h) (CD11c<sup>+</sup>CD40<sup>+</sup>CD86<sup>+</sup>) in lymph nodes from mice at 3 days after various treatments ( $n = 3$ ). (i, j) Representative flow cytometry plots (i) and quantification of cytotoxic T cells (j) (CD45<sup>+</sup>CD3<sup>+</sup>CD8<sup>+</sup>) in lymph nodes from mice at 7 days after various treatments ( $n = 3$ ). (k) Representative flow cytometry plots and quantification of CD4<sup>+</sup> T cells (gated on CD45<sup>+</sup>CD3<sup>+</sup>) in lymph nodes from mice at 7 days after various treatments ( $n = 3$ ). (l) CT26 tumor-bearing mice were analyzed on day 7 after different treatments by flow cytometry for the frequency of CD107a<sup>+</sup> NK cells within tumor-draining lymph nodes and spleen. (m–o) Quantification of mature DCs (CD11c<sup>+</sup>CD40<sup>+</sup>CD86<sup>+</sup>) (m), CD8<sup>+</sup> T cells (gated on CD45<sup>+</sup>CD3<sup>+</sup>) (n), and CD4<sup>+</sup> T cells (gated on CD45<sup>+</sup>CD3<sup>+</sup>) (o) in spleen from mice. (p) Surviving mice were rechallenged with CT26 tumor cells on day 60. Statistical significance was calculated via one-way ANOVA with Tukey's test: \* $p < 0.05$ ; \*\* $p < 0.01$ ; \*\*\* $p < 0.001$ ; \*\*\*\* $p < 0.0001$ .

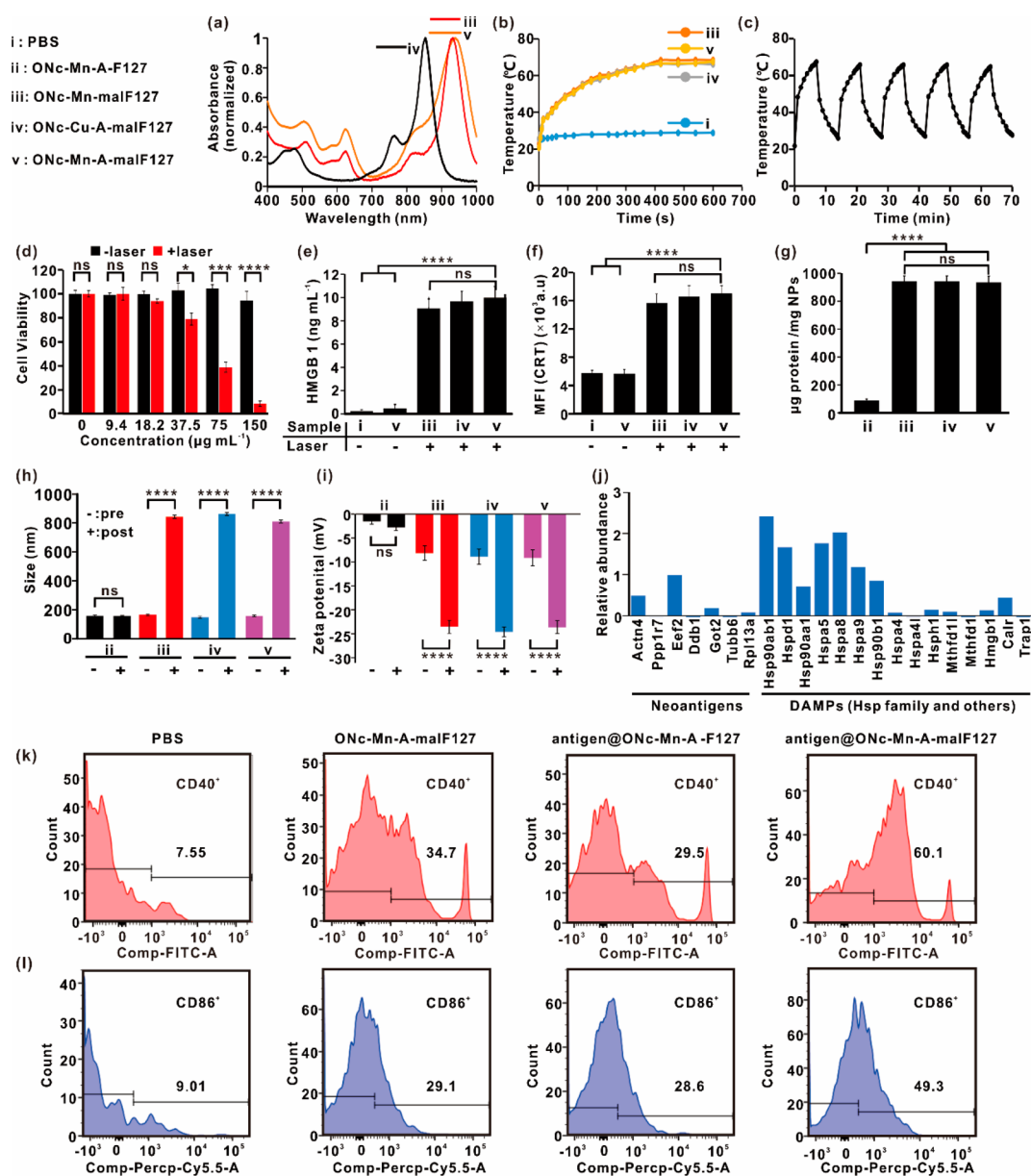


**Figure 5.** Photothermal properties of ONc-Mn-A-malF127 nanoparticles and photoinduced immunogenic cell death in vitro. Groups are as follows: (i) PBS, (ii) ONc-Mn-A-F127, (iii) ONc-Mn-A-malF127, (iv) ONc-Cu-A-malF127, (v) ONc-Mn-A-malF127. (a) UV-vis absorbance spectra of the formulations iii–v. (b) Photothermal effect of different formulations iii–v with PBS as a control. ONc concentration is 150  $\mu\text{g mL}^{-1}$  for samples iii–v, under NIR irradiation with the wavelength at 940 nm (for iii and v) or 860 nm (for iv), 1.0 W  $\text{cm}^{-2}$ . (c) Reversibility of temperature change of the ONc-Mn-A-malF127 (150  $\mu\text{g mL}^{-1}$ ) under on–off NIR irradiation cycles (940 nm, 1.0 W  $\text{cm}^{-2}$ ). (d) Viability of CT26 cells treated with formulation v, with or without laser irradiation. (e) Extracellular release of HMGB1 from CT26 cells after treatments as indicated. (f) CRT exposure on CT26 cells after indicated treatments. (g) Quantification of protein captured by various nanoparticles by BCA assay. (h) Size of ONc-Mn-A-F127, ONc-Mn-malF127, ONc-Cu-A-malF127, or ONc-Mn-A-malF127 before and after antigen capture. (i) Zeta potential of ONc-Mn-A-F127, ONc-Mn-malF127, ONc-Cu-A-malF127, or ONc-Mn-A-malF127 before and after antigen capture. (j) Relative abundance of TDPAs captured by ONc-Mn-A-malF127 measured by mass spectrometry. (k, l) Quantification of CD40<sup>+</sup> (k) and CD86<sup>+</sup> (l) expression via flow cytometry after BMDCs were treated with various samples as indicated. Statistical significance was calculated via one-way ANOVA with Tukey's test: \* $p < 0.05$ ; \*\* $p < 0.01$ ; \*\*\* $p < 0.001$ ; \*\*\*\* $p < 0.0001$ .

injection of different formulations (Figure 4c). Recently, increasingly potent Mn-based biomaterials have been developed, and suppressed tumor growth was achieved by three intravenous injections (10  $\mu\text{g}$  OVA and 36  $\mu\text{g}$   $\text{Mn}^{2+}$  for each injection per mouse)<sup>25</sup> or three injections of CDN-Mn<sup>2+</sup> nanoparticles (20  $\mu\text{g}$  CDA and 10  $\mu\text{g}$   $\text{Mn}^{2+}$  for each injection per mouse).<sup>26</sup> However, the results presented here showed that fewer intravenous injections of ONc-Mn-A-malF127 with

lower dose (each containing 10  $\mu\text{g}$  of ABZI and 10  $\mu\text{g}$  of  $\text{Mn}^{2+}$ ) could achieve similar therapeutic effects, although other experimental differences could also contribute. ONc-Mn-A-malF127 significantly inhibited CT26 tumor growth, and 50% of tumors were eliminated after two injections, while PBS, free  $\text{Mn}^{2+}$  + ABZI, and ONc-Mn-malF127 had no significant effect on tumors (Figure 4d–f). Although intravenous injection of ONc-Cu-A-malF127 can slow down tumor growth owing to

the STING agonist, it could not eradicate tumors as effectively as the combination of Mn and ABZI, indicating the enhanced antitumor effect of Mn<sup>2+</sup> and ABZI STING agonist (Figure 4d–f).

To elucidate the mechanism of STING pathway activation for superior antitumor effects, we next tested immune responses activated by immune cells in lymph nodes and spleen. Considering that DCs play an important role in activating innate and adaptive immunity, we hypothesized that the ONc-Mn-A-malF127-mediated cGAS-STING pathway associated with IFN $\beta$  secretion may promote the maturation of DCs, which then migrate from tumors to tumor-draining lymph nodes (TDLNs) for subsequent T cell activation. To test this hypothesis, we tested DC maturation in TDLNs by flow analysis (Figure 4g,h). Surprisingly, ONc-Mn-A-malF127 promoted the maturation of DCs, and the percentage of mature DCs (CD11c<sup>+</sup>CD40<sup>+</sup>CD86<sup>+</sup>) was as high as 53.8%, about 5 times higher than that of PBS, free Mn<sup>2+</sup> + ABZI, and ONc-Mn-malF127. Although ONc-Cu-A-malF127 still promoted DC maturation to a certain extent (33.4%), it was much lower than ONc-Mn-A-malF127, owing to the presence of Mn<sup>2+</sup> that potentiates STING agonist activity and IFN-I response (Figure 4g,h). Most importantly, type I IFNs enhanced the ability of cDC1s to activate CD8<sup>+</sup> T cells through upregulating co-stimulatory molecules (including CD40 and CD86).<sup>12</sup> Activation of antitumor immune response was then verified by measuring the populations of helper T cells (CD4<sup>+</sup>) and CD8<sup>+</sup> T cells in TDLNs. Compared with PBS, free Mn<sup>2+</sup> + ABZI, and ONc-Mn-malF127 groups, ONc-Cu-A-malF127 slightly activated the STING pathway due to the STING agonist ABZI, and some CD8<sup>+</sup> T cells and CD4<sup>+</sup> T cells were also activated (Figure 4i–k). But the populations CD8<sup>+</sup> T cells and CD4<sup>+</sup> T cells (gated on CD45<sup>+</sup>CD3<sup>+</sup>) in the ONc-Mn-A-malF127 group were the largest (40.9% and 44.3%), 4 times higher than the PBS and free Mn<sup>2+</sup> + ABZI groups and 2 times higher than the ONc-Mn-malF127 and ONc-Cu-A-malF127 groups, suggesting that the synergistic activation of the STING pathway promotes the effective activation of antitumor immune responses in vivo (Figure 4i–k).

Tumor cells may evade CD8<sup>+</sup> T cell response via selective or complete loss of major histocompatibility complex (MHC) class I expression.<sup>5</sup> Natural killer (NK) cells are innate cytotoxic lymphocytes that are important for killing tumor cells.<sup>51</sup> NK cells recognize cells that have lost MHC class I and increase adaptive immune responses to directly kill cells that have lost MHC-I expression.<sup>7</sup> Therefore, NK cell activation in TDLNs in vivo was also assessed by flow analysis. ONc-Mn-A-malF127 significantly promoted NK cell activation in TDLNs (gated on CD45<sup>+</sup>CD49b<sup>+</sup>CD3<sup>+</sup>CD107a<sup>+</sup>) (Figure 4l). This may be because Mn<sup>2+</sup> potentiates STING agonist activity and IFN-I response to produce abundant type I IFNs, which play central roles in NK cell maturation, homeostasis, and activation.<sup>52</sup> In addition to cGAS-STING pathway activation to induce strong antitumor immune responses in TDLNs, robust immune responses in spleen were also observed (Figure 4l–o and Figures S24–26), showing that the immune responses in the immune organs were effectively activated, contributing to tumor eradication. In addition, the survivors from the ONc-Mn-A-malF127 treatment group that were rechallenged with CT26 cells on day 60, and no tumor was observed during another 40 days (Figure 4p and Figure S27). Altogether, intravenous injection of ONc-Mn-A-malF127 not

only can kill tumor cells by activating CD8<sup>+</sup> T cells but also can kill MHC-I-deficient tumors by activating NK cells, demonstrating that Mn<sup>2+</sup> and STING agonists enhance cGAS-STING pathway-triggered metal immunity by the action of NK cells and cytotoxic T cells.

Although intravenous injection of ONc-Mn-A-malF127 can induce strong innate immunity and adaptive immunity showing potential antitumor effect with two doses, the primary tumor cannot be completely eradicated, and it is possible for tumor metastasis to occur, complicating the major clinical scenario with poor abscopal effect. This may be because after systemic administration, the vaccine is enriched in the tumor site, but a large number of tumor cells rather than tumor-infiltrating DCs exist in the tumor site, resulting in the inability of the vaccine to be effectively taken up by DCs.<sup>31,32</sup> Therefore, we next investigated the immunogenic cell death induced by external stimulus to enhance future tumor eradication.

**Photoinduced Antigen Capture in Vitro.** ONc has been reported as a promising NIR photosensitizer with high photothermal conversion efficiency.<sup>53–55</sup> With the chelation of metal in the center, ONc-Cu-A-malF127 nanoparticle aqueous solution has similar absorption as ONc in organic solvent at around 860 nm, whereas ONc-Mn-A-malF127 exhibited red shift to around 940 nm, close to the NIR-II region (Figure 5a), because the chelation of Mn<sup>2+</sup> in ONc caused red-shifted absorbance from 860 to 940 nm but Cu<sup>2+</sup> did not (Figure S23b). The NIR photothermal properties of ONc-Mn-A-malF127 nanomicelles are displayed in Figure S28a,b. After irradiation using a 940 nm laser with a power density of 1.0 W cm<sup>-2</sup> for 7 min, the temperature of different ONc-containing formulations including ONc-Mn-malF127, ONc-Mn-A-malF127, and ONc-Cu-A-malF127 micelle, but not PBS, reached as high as 66 °C (Figure 5b and Figure S28c). The same temperature change trend was observed after 5 thermal cycles for ONc-Mn-A-malF127 aqueous solution, showing excellent photothermal reversibility (Figure 5c). The photothermal conversion rate of ONc-Mn-A-malF127 was calculated to be around 70% through the cooling process (Figure S29). Also, the increase of temperature to 70 °C did not affect the activity of the STING agonist ABZI, generating the same amount of IFN $\beta$  before and after laser treatment. (Figure S30) These results all show that ONc-Mn-A-malF127 has excellent photothermal properties and photothermal stability, showing its application potential in photothermal therapy.

Based on the attractive photothermal properties of the micelles, their photothermal therapeutic effects were investigated in vitro. After CT26 cells were treated with ONc-Mn-A-malF127 + laser, cell viability was tested using a CCK8 kit (Figure 5d). ONc-Mn-A-malF127 + laser caused 92% cell death at a ONc-Mn-A-malF127 dose of 150  $\mu$ g mL<sup>-1</sup>, with laser power density of 1.0 W cm<sup>-2</sup> and an irradiation time of 7 min. In contrast, with no laser irradiation, no obvious toxicity was observed (Figure 5d). This shows that ONc-Mn-A-malF127 not only has good tumor cell killing effect after laser irradiation but also has good biocompatibility. The dying CT26 tumor cells release a large amount of high mobility group protein B1 (HMGB1) as “find me” signals to induce DC maturation, and their surface exposes calreticulin (CRT) as “eat me” signal to initiate DC uptake and processing of antigens.<sup>33,35</sup> Therefore, HMGB1 was assessed in the culture of CT26 tumor cells (Figure 5e). Compared with PBS and

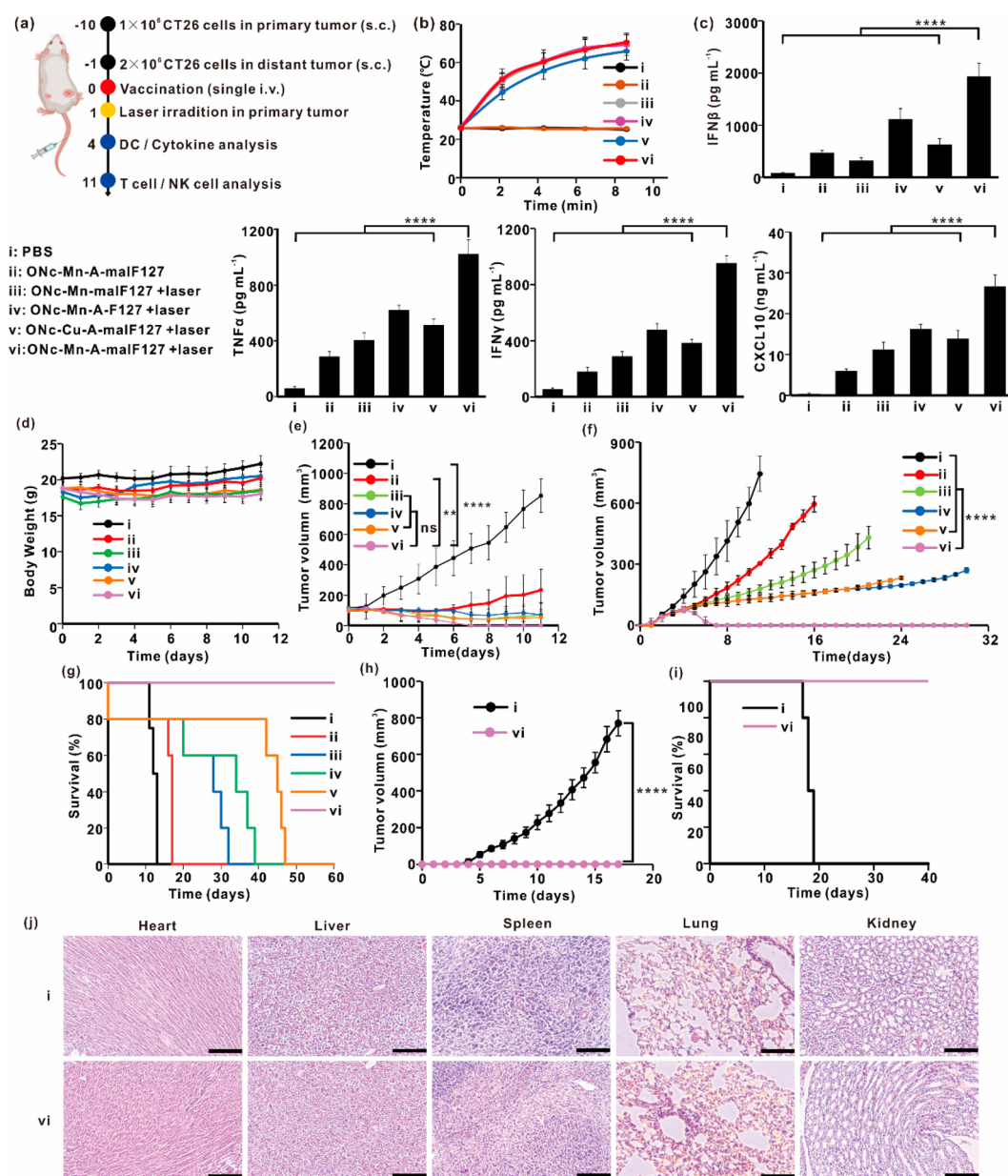


**Figure 6.** In vivo antitumor efficacy of ONc-Mn-A-malF127 by photoinduced in situ antigen capturing and metalloimmunotherapy. (a) Treatment scheme for antitumor efficacy of ONc-Mn-A-malF127 after iv administration of different formulations: (i) PBS, (ii) ONc-Mn-A-malF127, (iii) ONc-Mn-malF127 + laser, (iv) ONc-Mn-A-F127 + laser, (v) ONc-Cu-A-malF127 + laser, (vi) ONc-Mn-A-malF127 + laser. CT26 tumor-bearing BALB/c mice were treated intravenously with various formulations containing 10  $\mu\text{g}$  of ABZI, 10  $\mu\text{g}$  of  $\text{Mn}^{2+}$  and 50  $\mu\text{g}$  of ONc per mouse on day 0. (b) Tumor temperature of CT26-tumor-bearing mice injected with formulations after 940 nm (for groups ii, iii, iv, and vi) or 860 nm (for groups i and v) laser irradiation (10 min, 1.0  $\text{W cm}^{-2}$ ); IR thermal images are shown in Figure S32. (c) Serum cytokines were measured by ELISA 3 days after laser irradiation in primary tumor. Statistical significance was calculated via one-way ANOVA with Tukey's test: \* $p < 0.05$ ; \*\* $p < 0.01$ ; \*\*\* $p < 0.001$ ; \*\*\*\* $p < 0.0001$ . (d) Body weight of mice during various treatments. (e, f) Growth curves of primary tumors (e) and distant tumors (f) in CT26 tumor-bearing mice after different treatments ( $n = 4$ ). (g) Survival curve of treated mice. (h, i) Surviving mice were rechallenged with CT26 tumor cells on day 60. (j) Hematoxylin and eosin analysis of major organs after systemic injections of different formulations, Scale bars = 50  $\mu\text{m}$ . Statistical significance of tumor growth was calculated via two-way ANOVA with Tukey's test.

ONc-Mn-A-malF127, CT26 treated with ONc-Mn-malF127 + laser, ONc-Cu-A-malF127 + laser, and ONc-Mn-A-malF127 + laser released a large amount of HMGB1, which was about 10 times that of the control group (Figure 5e). Similarly, CT26 cells treated with ONc-Mn-malF127 + laser, ONc-Cu-A-malF127 + laser, and ONc-Mn-A-malF127 + laser possessed a large amount of CRT on the surface (Figure 5f and Figure S15d), which leads to DC uptake and antigen presentation in

the tumor microenvironment. These results show that ONc-Mn-A-malF127 can effectively kill CT26 cancer cells and induce a stronger immune response.

Maleimide-based nanoparticles have shown promise for effectively capturing tumor-derived protein antigens (TDPAs) released from dying cancer cells and delivering them to antigen-presenting cells (APCs) to initiate immune response.<sup>36</sup> Therefore, F127 was chemically modified with maleimide and

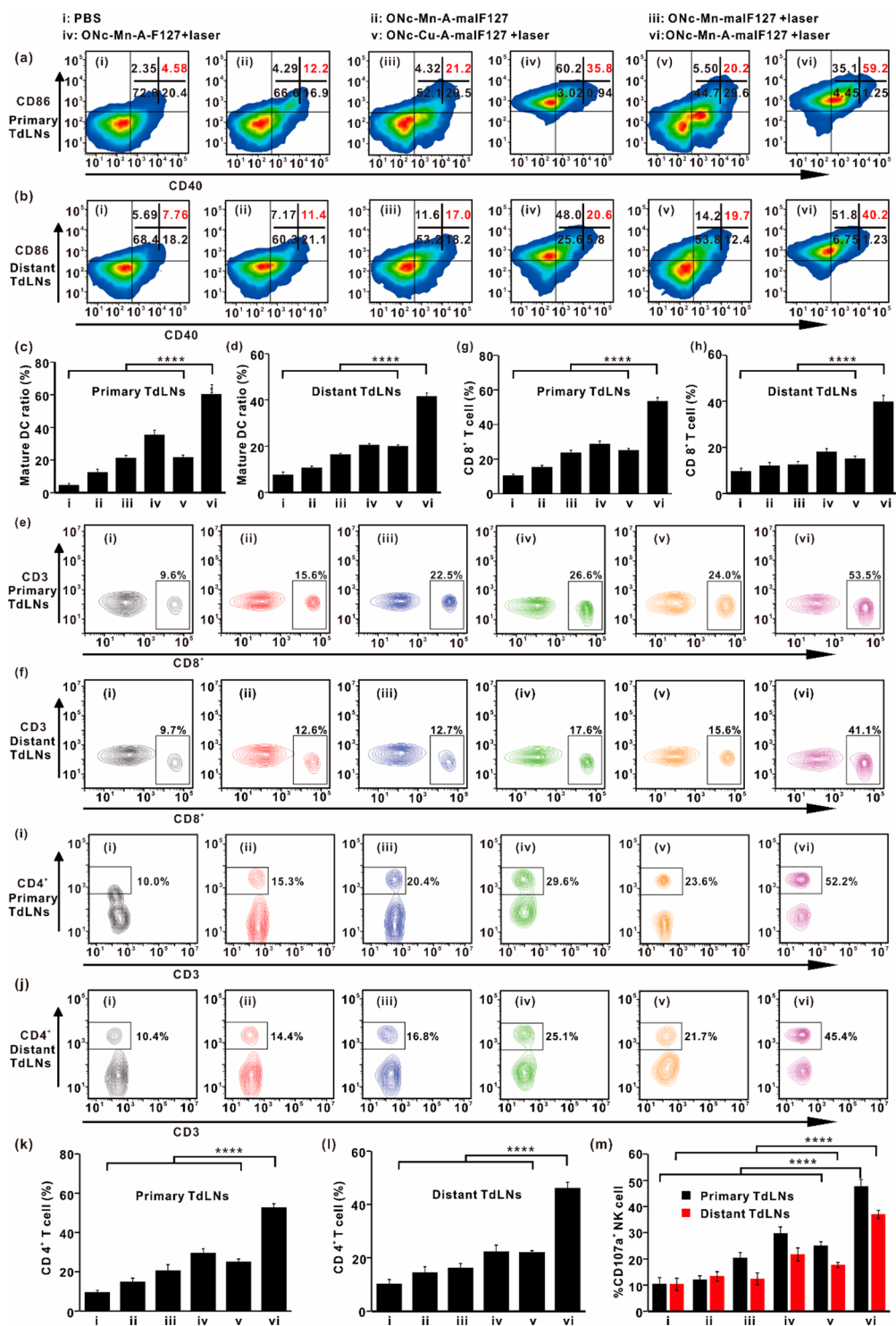


**Figure 7.** In vivo immune response after photo-metalloimmunotherapy treatment. CT26 tumor-bearing BALB/c mice were treated intravenously with various formulations: (i) PBS, (ii) ONc-Mn-A-malF127, (iii) ONc-Mn-malF127 + laser, (iv) ONc-Mn-A-F127 + laser, (v) ONc-Cu-A-malF127 + laser, (vi) ONc-Mn-A-malF127 + laser. Injection dose: 10  $\mu$ g of ABZI, 10  $\mu$ g of Mn<sup>2+</sup>, and 50  $\mu$ g of ONc on day 0. (a, b) DC maturation measurements via flow cytometry after cells in primary (a) and distant (b) TdLNs were collected and stained with CD11c, CD40 and CD86 on day 3. (c, d) Percentage of mature DCs (gated on CD11c<sup>+</sup>) in tumor-draining lymph nodes (c) and distant tumor-draining lymph nodes (d) on day 3 after indicated treatments. (e–h) Representative flow cytometry plots and quantitative analysis of CD8<sup>+</sup> T cells (gated on CD3<sup>+</sup> T cells) in the tumor-draining lymph nodes (e, g) and distant tumor-draining lymph nodes (f, h) on day 7 after different treatments. (i–l) Representative flow cytometry plots and quantitative analysis of CD4<sup>+</sup> T cells (gated on CD3<sup>+</sup> T cells) in the primary tumor-draining lymph nodes (i, k) and distant tumor-draining lymph nodes (j, l) on day 7 after different treatments as indicated. (m) CT26 tumor-bearing mice were analyzed on day 7 after different treatments by flow cytometry for the frequency of CD107a<sup>+</sup> NK cells in primary and distant tumor-draining lymph nodes. Statistical significance was calculated via one-way ANOVA with Tukey's test: \**p* < 0.05; \*\**p* < 0.01; \*\*\**p* < 0.001; \*\*\*\**p* < 0.0001.

used as both carrier of ONc-Mn-A-malF127 and scaffold for capturing antigen of TDPAs. Interestingly, after maleimide modification, the encapsulation efficiency of ONc-Mn-A in F127 increased from 50% to 87% (Figure S31) for reasons that are not clear. To demonstrate the capability of maleimide-modified F127 for capturing TDPAs, a control group of ONc-Mn-A encapsulated pristine F127 nanoparticles, termed ONc-Mn-A-F127, was used. After laser irradiation to induce immunogenic cell death (ICD), antigen capture by ONc-Mn-A-malF127 was studied. The hydrodynamic particle size and the zeta potential significantly decreased (Figure 5h–i). In comparison, the hydrodynamic particle size and the zeta potential of ONc-Mn-A-F127 did not change significantly. Quantitative analysis with a bicinchoninic acid (BCA) protein assay kit showed that ONc-Mn-A-malF127 captured high levels of protein ( $940 \mu\text{g mg}^{-1}$ ) compared to ONc-Mn-A (Figure 5g). The proteins captured by ONc-Mn-A-malF127 were quantified using mass spectrometry, and 7 neoantigens and 15 TDPAs were identified as shown in Figure 5j and Table S2. ONc-Mn-malF127 and ONc-Cu-A-malF127 exhibited similar antigen capture ability (Figure 5g–i). We further incubated antigen-bound ONc-Mn-A-malF127 (antigen@ONc-Mn-A-malF127) with BMDCs and found that antigen@ONc-Mn-A-malF127 induced BMDC maturation, indicated by the significantly increased co-stimulatory CD40 and CD86 expression levels (Figure 5k,l). Taken together, these results demonstrate that ONc-Mn-A-malF127 exhibited excellent ability to capture TDPAs to activate APCs.

**In Vivo Primary and Distant Tumor Treatment by Metalloimmunotherapy Coupled with Photothermal Therapy and Its Induction of In Situ Capturing of Antigens.** Based on the above results, bilateral tumor models were established in order to study the antitumor efficacy of photothermal metalloimmunotherapy and the abscopal effect in vivo. CT26 cancer cells were injected subcutaneously (sc) into the right side of mice, and 9 days later CT26 cancer cells were injected sc on the left side of the same mice (Figure 6a). After intravenous injection of PBS (i), ONc-Mn-malF127 (ii), ONc-Mn-A-F127 (iii), ONc-Cu-A-malF127 (iv), and ONc-Mn-A-malF127 (v) (containing  $10 \mu\text{g}$  of ABZI,  $10 \mu\text{g}$  of  $\text{Mn}^{2+}$ , and  $50 \mu\text{g}$  of ONc) for 24 h,  $940 \text{ nm}$  (for i, iii, v) or  $860 \text{ nm}$  (for iv) laser irradiation was applied to the primary tumors ( $7 \text{ min}$ ,  $1.0 \text{ W cm}^{-2}$ ). Upon photoirradiation, the temperature of primary tumors in the groups of ONc-Mn-malF127, ONc-Mn-A-F127, ONc-Cu-A-malF127, and ONc-Mn-A-malF127 increased to about  $70 \text{ }^\circ\text{C}$ , exhibiting excellent photothermal performance (Figure 6b and Figure S32). Three days after irradiation, blood from the treated mice was collected for the measurement of immune cell-derived cytokines such as  $\text{IFN}\beta$ ,  $\text{TNF}\alpha$ ,  $\text{IFN}\gamma$ , and  $\text{CXCL10}$ . We found that ONc-Mn-A-malF127-mediated PTT yielded the highest levels of the immune cell-derived cytokines ( $\text{IFN}\beta$ ,  $\text{TNF}\alpha$ ,  $\text{IFN}\gamma$ , and  $\text{CXCL10}$ ) (Figure 6c). The massive production of cytokines suggested that the combination of  $\text{Mn}^{2+}$  and ABZI effectively activated cGAS-STING pathway. Compared to ABZI alone,  $\text{Mn}^{2+}$  enhanced the agonist activity of ABZI, amplifying cGAS-STING pathway activation and  $\text{IFN-I}$  response.  $\text{IFN}\beta$  secreted from immune cells acts as a downstream signal of the cGAS-STING pathway, which is regarded as a bridge between innate and adaptive immunity. Type I IFNs ( $\text{IFN}\beta$ ) can recruit a large number of  $\text{CD8}^+$  T cells through chemokine  $\text{CXCL10}$ , amplify natural killer cell cytotoxicity, and suppress the activity of

protumorigenic immune cells (such as myeloid-derived suppressor cells or regulatory T cells).<sup>56</sup>

The body weight and tumor growth (primary and distant) of mice were continuously monitored for 30 days after photoirradiation. During this period, there was no significant decrease in the body weight of the mice, suggesting that there is no significant short-term systemic toxicity or phototoxicity after systemic injection of different formulations (Figure 6d). Compared with PBS, the growth of primary tumor after ONc-Mn-A-malF127 treatment without laser irradiation was still significantly inhibited, and the cure rate reached 25% (Figure 6e and Figure S33). This shows that even a single injection of  $\text{Mn}^{2+}$  and ABZI can induce metal immune responses to retard tumor growth, further illustrating the potential of metalloimmunotherapy. In addition, 75% or 100% of primary tumors in the groups of ONc-Mn-malF127 + laser, ONc-Mn-A-F127 + laser, ONc-Cu-A-malF127 + laser, and ONc-Mn-A-malF127 + laser were completely eradicated after laser irradiation compared to no laser treatment (PBS and ONc-Mn-A-malF127) because of the strong photothermal performance of ONc to ablate CT26 tumor cells. The distant tumor in the PBS, ONc-Mn-A-malF127, and ONc-Mn-malF127 + laser groups increased rapidly because no STING agonist ABZI was used. Although the growth rate of the distant tumor in the ONc-Mn-A-F127 + laser and ONc-Cu-A-malF127 + laser groups was significantly inhibited, tumors still grew and no eradication was observed due to lack of ABZI for effective STING pathway activation or lack of the amplification effect by Mn. In contrast, distant tumors treated with ONc-Mn-A-malF127 + laser were completely eradicated, and the cure rate reached 100% (Figure 6f,g and Figure S34). Moreover, the survivors from the ONc-Mn-A-malF127 + laser treatment group remained resistant to CT26 tumor rechallenge performed on day 60 (Figure 6h,i and Figure S35), showing the induction of antitumor memory responses. Three days after laser irradiation, blood was collected for the analysis of serum chemistry and liver function. Main organs including heart, liver, spleen, lung, and kidney were also collected for histological hematoxylin and eosin (H&E) staining. As shown in Figure S36, serum chemistry profile and liver indexes have no difference between the mice treated with ONc-Mn-A-malF127 and PBS, indicating that intravenous vaccination and laser irradiation did not induce overt toxicity in vivo (Figure S36). Major organs of the mice treated with various samples were examined by H&E staining analysis, and no abnormal histological conditions (necrosis, inflammation, or structural changes) or other abnormality was observed (Figure 6j and Figure S37). These results indicate that the nanovaccine ONc-Mn-A-malF127 did not cause acute toxicity in vivo, at least in mice. Although other promising STING agonist studies showed that ICD-based Mn activation of the STING pathway can effectively suppress tumor growth by multiple intravenous administrations combined with radiotherapy<sup>32</sup> or sonodynamic therapy,<sup>57</sup> our results showed that ICD-based metalloimmunotherapy using ONc-Mn-A-malF127 nanovaccine using a single dose achieved complete eradication of primary and distant tumors.

To further shed light on the mechanism of distal antitumor action, we investigated the activation of systemic immune responses after treatment with various formulations. We first analyzed DC maturation in primary and distant TdLNs (Figure 7a–d) and in spleen (Figure S38) by flow cytometry. The ONc-Mn-A-malF127 + laser treatment induced the

highest level of mature DCs ( $CD11c^+CD40^+CD86^+$ ) in primary TdLNs, which reached up to 59.2%. However, the percentage was only 4.58%, 12.2%, 21.2%, 35.8%, and 20.2% in the groups of PBS, ONc-Mn-A-malF127, ONc-Mn-malF127 + laser, ONc-Mn-A-F127 + laser, and ONc-Cu-A-malF127 + laser, respectively, all much lower than 59.2% (Figure 7a,c). Similarly, the percentage of mature DCs in the group ONc-Mn-A-malF127 + laser was as high as 40.2% in distant TdLNs, which was at least 2 times that in other groups (Figure 7b,d). This is because tumor-derived antigens (TDPAs and neoantigens) could be generated from the necrotic/apoptotic tumor cells induced by ONc-Mn-A-malF127 based PTT, resulting in recruitment of DCs to the tumor site, which circumvents the problem of only a small number of DCs existing in the tumor site for sufficient phagocytosis of vaccine nanoparticles. After these antigens (including TDPAs and neoantigens) were captured by the maleimide on the ONc-Mn-A-malF127 surface, APCs such as DCs were also recruited to the tumor site.<sup>38</sup> After taking up antigen, the mature DCs stimulated the proliferation and activation of naive T cells via type I IFN response.<sup>58</sup>  $CD8^+$  T cells play an essential role in directly killing cancer cells and activating antitumor immunity response;  $CD4^+$  T cells are critical to regulating adaptive immunities.<sup>59,60</sup> Thus, the populations of  $CD8^+$  and  $CD4^+$  T cells in both primary and distant TdLNs were measured by flow cytometry. The significant infiltration of these two types of T cells in distant tumors plays a key role in distant tumor inhibition. The infiltration of  $CD8^+$  T cells in the primary and distant TdLNs notably reached 53.5% and 41.1%, respectively, in the group ONc-Mn-A-malF127 + laser, which was the highest among all the experimental groups, at least 2 times higher than other groups (Figure 7e–h). The ONc-Mn-A-malF127 + laser treatment also increased the percentage of  $CD4^+$  T cells in TdLNs, where T cells were educated by mature DCs (Figure 7i–l).  $CD8^+$  cytotoxic T cells and  $CD4^+$  T helper cells were effectively primed after the cGAS-STING-IFN-I pathway of immune cells was activated in TdLNs and type I IFN ( $IFN\beta$ ) was generated. Similarly, the populations of both  $CD8^+$  cytotoxic T cells and  $CD4^+$  T helper cells in spleens were also most elevated after photothermal therapy mediated by ONc-Mn-A-malF127 (Figures S38–40). Additionally, NK cell activation was further analyzed, and we found that photo-metalloimmunotherapy using ONc-Mn-A-malF127 can also effectively activate NK cells to kill tumor cells that evade T cell responses (Figure 7m). These data validate that ONc-Mn-A-malF127 could stimulate superior systemic  $CD8^+$  T cell and NK cell immune responses with abscopal effect for potent cancer photothermal metalloimmunotherapy over other monotherapies.

## CONCLUSION

In summary, we designed a metal-coordinated micelle nanovaccine (ONc-Mn-A-malF127), which induces DC maturation and contributes to  $CD8^+$  T cell and NK cell activation. ONc-Mn-A-malF127 was designed to enhance innate and adaptive immune responses based on the synergy of ABZI and Mn, in addition to ICD-induced immunotherapy. The PTT-mediated ICD effect can effectively destroy primary tumors, releasing DAMPs and tumor antigens (including neoantigens) from dying primary tumor cells, which are effectively captured by maleimide groups on the surface of F127, and the as-formed *in situ* nanovaccine is phagocytosed by DCs to also co-deliver  $Mn^{2+}$  and the STING agonist ABZI.

$Mn^{2+}$  significantly amplifies ABZI activity and promotes cGAS-STING activation. Our findings suggest that substantial canonical type I IFN was produced by this approach. A single systemic administration and treatment promotes  $CD8^+$  T cell and NK cell activation to kill  $CD8^+$  T cell-sensitive tumors and  $CD8^+$  T cell-resistant tumors, respectively. This treatment approach also achieved complete eradication of primary and distant tumors. Taken together, the metal vaccine ONc-Mn-A-malF127 used for ICD-based metalloimmunotherapy shows potential for anticancer immunotherapy.

## MATERIALS AND METHODS

### Synthesis of ABZI. See Supporting Information.

**Assessing Metal Ion and STING Agonist ABZI Activation of cGAS-STING Pathway to Enhance IFN-I Response.** Mouse BMDC extraction and culture were performed according to previously reported methods.<sup>61</sup> In order to screen different metal ions and the STING agonist ABZI to modulate the cGAS-STING pathway, we used 6-well plates containing  $1 \times 10^6$  cells, and metal ions ( $MnCl_2$ ,  $FeCl_2$ ,  $ZnCl_2$ ,  $CuCl_2$ ,  $NiCl_2$ ,  $CoCl_2$ ) at different concentrations (0, 250, 1000  $\mu M$ ) were added with 4  $\mu M$  ABZI. After 24 h incubation at 37 °C in a 5%  $CO_2$  incubator, the supernatant was used for IFN $\beta$  ELISA kit detection (Solarbio, Beijing, China), and cells were used for flow cytometry analysis of BMDC maturation. For staining, BMDCs were incubated with APC-anti-mouse CD11c antibody, FITC-anti-mouse CD40 antibody, and PerCP-Cy5.5-anti-mouse CD86 antibody (Biolegend, California, America) on ice for 40 min and washed twice with PBS. BMDCs were resuspended with 500  $\mu L$  of PBS for flow cytometry analysis (Becton Dickinson FACS Aria III); the data were analyzed using FlowJo software.

**Synthesis and Characterization of ONc-Mn-ABZI Coordination Nanoparticles.** ABZI (1.435 mg, 0.02 mmol) and ONc (2.5 mg, 0.04 mmol) were dissolved in THF (2 mL).  $MnCl_2$  THF solution (5 mg  $mL^{-1}$ , 500  $\mu L$ ) was added to 1 mg  $mL^{-1}$  ABZI and ONc solution in a 20:2:1 ( $Mn^{2+}/ONc/ABZI$ , n/n/n) ratio under vigorous stirring. After the mixture was sonicated for 5 min and subsequently stirred at room temperature for 24 h, this THF solution (100  $\mu L$ ) was rapidly injected into 5% maleimide-modified F127 aqueous solution (1 mL) and sonicated for 5 min, then subjected to ultracentrifugation with 100 000 molecular weight cut off at low temperature (4 °C) three times to obtain ONc-Mn-A-malF127 coordination nanoparticles.

The absorbance of ONc and fluorescence of ABZI in ONc-Mn-A-malF127 coordination nanoparticles were determined by UV absorbance at 940 nm using a microplate reader (excitation = 324 nm, emission = 436 nm). The amount of  $Mn^{2+}$  was determined by inductively coupled plasma optical emission spectrometry (ICP-OES) (iCAP7000 series). The morphology of polymers was observed using a transmission electron microscope (JEM-F200, JEOL) and Zeiss thermal scanning electron microscope (Sigma, 300). The size and surface charge of the ONc-Mn-A-malF127 coordination polymers were measured using a Zetasizer (Nano ZS).

**In Vitro Photothermal Properties of ONc-Mn-A-malF127.** To study the photothermal properties of ONc-Mn-A-malF127, a series of ONc-Mn-A-malF127 with different concentrations (0, 37.5, 75, 150, 300  $\mu g mL^{-1}$ ) of ONc were placed in a 1.5 mL EP tube and irradiated with a 940 nm laser (1.0  $W cm^{-2}$ ) for 10 min. ONc-Mn-A-malF127 (150  $\mu g mL^{-1}$ ) was irradiated with a series of 940 nm lasers of different powers (0, 0.6, 1.0, 1.5  $W cm^{-2}$ ) for 10 min. For photostability test, ONc-Mn-A-malF127 solution ( $[ONc] = 150 \mu g mL^{-1}$ ) was irradiated with 940 nm laser (1  $W cm^{-2}$ ) for 7 min, followed by natural cooling to room temperature for another 7 min, totaling 5 cycles. For comparison of photothermal properties of various samples, 1 mL of various samples (PBS, ONc-Mn-malF127, ONc-Cu-A-malF127, ONc-Mn-A-malF127) at the same concentration ( $ONc = 150 \mu g mL^{-1}$ ) were treated with 940 nm laser irradiation (1.0  $W cm^{-2}$ ) for 7 min. All temperature changes during laser irradiation were detected with infrared thermal cameras.

**In Vitro Anticancer Therapy.** CT26 cancer cells ( $5 \times 10^4$ ) were seeded in 96-well plates and incubated overnight in a 5% CO<sub>2</sub> incubator. Different concentrations of ONc-Mn-A-malF127 nanoformulations (ONc = 0, 9.4, 18.2, 37.5, 75, 150  $\mu\text{g mL}^{-1}$ ) were added for incubation for 4 h. After cells were treated with or without 940 nm laser irradiation ( $1.0 \text{ W cm}^{-2}$ , 7 min), cells were incubated again for 20 h, and cells were washed twice with PBS. Then freshly prepared CCK-8 (Solarbio, Beijing, China) working solution (100  $\mu\text{L}$  of 1640 medium and 10  $\mu\text{L}$  of CCK-8 reagent) was added to each well, and cells were incubated for 2 h. After incubation, the plate was measured on a microplate reader to read the absorbance at 450 nm. Cell viabilities were calculated as the ratio of the absorbance of cells with various treatments to that of the control cells without any treatments. Laser-irradiated cells were incubated with anti-calreticulin–Alexa Fluor 594 conjugate (Cell Signaling Technology, Boston, America) for 60 min on ice. The cells were washed twice with PBS and used to analyze the fluorescence intensity of CRT protein by fluorescence microscopy and flow cytometry. In addition, HMGB1 secreted by the treated CT26 cancer cells in 1640 medium was detected with a HMGB1 ELISA kit according to the protocol provided by manufacturer.

**Characterization of Antigens Captured by Different Samples in Vitro.** After  $1 \times 10^5$  CT26 cells were incubated with various samples (ONc-Mn-A-F127, ONc-Mn-malF127, ONc-Cu-A-malF127, ONc-Mn-A-malF127, ONc = 150  $\mu\text{g mL}^{-1}$ , ABZI = 2  $\mu\text{M}$ , metal ion = 15  $\mu\text{M}$ ) for 6 h in a 24-well plate, the medium was aspirated, and cells were washed twice with PBS. CT26 cells were irradiated with a 940 nm laser for 7 min, and then incubated with 1640 medium without FBS for 48 h. After incubation, cell supernatants were collected and centrifuged to remove all insoluble cell lysates to obtain antigen-containing cell supernatants. ONc-Mn-A-malF127 was incubated with cell supernatant again in a shaking incubator at 37 °C for 12 h and then subjected to centrifugation, washed three times with PBS, and then resuspended in PBS. A series of samples were evaluated with a Zetasizer (Nano ZS) to determine hydrodynamic diameter distribution and zeta potential before and after antigen capture. The antigens attached to ONc-Mn-A-malF127 were determined by liquid chromatography/tandem mass spectroscopy (LC/MS/MS). The neoantigens listed are based on previously reported neoantigen species.<sup>62</sup> In addition, the nanoparticles after capturing protein (protein = 250  $\mu\text{g mL}^{-1}$ ) were incubated with  $1 \times 10^5$  BMDCs for 24 h for flow cytometry analysis of DC maturation.

**Western Blot Analysis.** BMDCs ( $2 \times 10^6$ ) were seeded in a 6-well plate and incubated overnight in a 5% CO<sub>2</sub> incubator; then various samples were added and incubated for 6 h. After incubation, DAPI lysate was added to the collected BMDCs for lysis for 20 min, and the proteins were collected by centrifugation. The protein and loading buffer were heated at 100 °C for 5 min to denature the protein. Samples (30  $\mu\text{L}$ : 24  $\mu\text{L}$  of protein solution and 6  $\mu\text{L}$  of loading buffer) were added to each well of 12% SDS-PAGE gels and electrophoresed at 80 V for 30 min and 120 V for 2 h, and the total protein mass in each well was adjusted to be consistent. Proteins bands in SDS-PAGE gels were then electrically transferred to PVDF membranes under 220 mA at 4 °C for 2.5 h and washed three times with  $1 \times$  TBST. After blocking with 5% (w/v) skim milk for 80 min, the membrane was incubated with a primary antibody [phospho-NF- $\kappa\text{B}$  p65 (pS536) (Cohesion), NF- $\kappa\text{B}$  p65 (Cohesion), phospho-IRF3 (pS396) (Cohesion), IRF3 (Cohesion), phospho-TBK1 (pS172) (Cohesion), TBK1 (Cohesion), or  $\beta$ -actin (Cohesion)] overnight at 4 °C followed by incubation with the relevant secondary antibody (goat anti-rabbit IgG, Cohesion). Protein bands were visualized by chemiluminescence imaging with SHSP/substrate.

**In Vitro DC Activation.** After BMDCs were incubated with different samples (PBS, free, ONc-Mn-malF127, ONc-Cu-A-malF127, ONc-Mn-A-malF127, ONc = 150  $\mu\text{g mL}^{-1}$ , metal ion = 15  $\mu\text{M}$ , ABZI = 2  $\mu\text{M}$ ) for 24 h, the cells and supernatant were separated by centrifugation (1900 rpm, 8 min). The supernatant was used for the quantification of IFN $\beta$  and TNF $\alpha$  with ELISA kits (Solarbio, Beijing, China). The cells were stained with flow antibodies, APC–anti-mouse CD11c antibody, FITC–anti-mouse CD40 antibody, and PerCP-

Cy5.5–anti-mouse CD86 antibody (Biolegend, California, America), and incubated on ice for 40 min. After incubation, they were washed twice with PBS and resuspended in 500  $\mu\text{L}$  of PBS for flow cytometry assay.

**In Vivo Metalloimmunotherapy in BALB/c Mice.** All animal procedures were approved by the Animal Experiment Ethics Committee at Tianjin University (permit number TJUE-2022-007). For tumor inoculation, CT26 cancer cells resuspended in PBS were injected subcutaneously on the right side of each female BALB/c mouse ( $1 \times 10^6$  per mouse, 6–8 weeks old). After 10 days, when the tumor volume reached about 100 mm<sup>3</sup>, 200  $\mu\text{L}$  of different formulations (PBS, free, ONc-Mn-malF127, ONc-Cu-A-malF127, ONc-Mn-A-malF127, 10  $\mu\text{g}$  of ABZI, 10  $\mu\text{g}$  of Mn<sup>2+</sup>, and 50  $\mu\text{g}$  of ONc) were injected intravenously. Five days later, a second dose of the same drug formulation was injected intravenously into the mice. Six hours after injection, mouse blood was drawn for cytokine assay. On the third and seventh days after the second injection, the mouse lymph nodes, spleens, and tumor tissues were removed for flow cytometry analysis of in vivo immune responses. The body weight and tumor size of the mice were monitored every day, and the tumor volume was calculated according to the formula tumor volume = (tumor length)  $\times$  (tumor width)<sup>2</sup>  $\times$  0.5.

For the rechallenge study, surviving BALB/c mice ( $n = 3$ ) after ONc-Mn-A-malF127 treatment were injected subcutaneously with  $1 \times 10^6$  CT26 cells (right flank) on day 60. Additional control mice ( $n = 3$ ) were implanted with the same tumor cells for comparison, followed by tumor volume measurement up to 40 days.

**In Vivo Photothermal Metalloimmunotherapy in BALB/c Mice.** For assessing photoinduced ICD based metalloimmunotherapy, CT26 cancer cells resuspended in PBS were injected subcutaneously on the right side of each female BALB/c mouse ( $1 \times 10^6$  per mouse, 6–8 weeks old) for the establishment of the primary tumor. After 9 days,  $1 \times 10^6$  CT26 tumor cells were injected subcutaneously into the left side of mice for the establishment of the distant tumor. One day after tumor inoculation, 200  $\mu\text{L}$  of different formulations (PBS, free, ONc-Mn-malF127, ONc-Cu-A-malF127, ONc-Mn-A-malF127, 10  $\mu\text{g}$  of ABZI, 10  $\mu\text{g}$  of Mn<sup>2+</sup> and 50  $\mu\text{g}$  of ONc) were injected intravenously. Twenty-four hours after injection, tumors of mice in photothermal immunotherapy groups were irradiated with 940 or 860 nm laser at  $1.0 \text{ W cm}^{-2}$  for 10 min. Tumor temperatures were monitored with an IR thermal camera. On the third and seventh days after all treatments were completed, the mouse lymph nodes, spleens, and tissues of primary and distant tumors were removed for flow cytometry analysis of in vivo immune responses. Tumor volumes of both primary and distant tumors and body weights of mice were measured every day for 30 days, and the tumor volume was calculated according to the formula tumor volume = (tumor length)  $\times$  (tumor width)<sup>2</sup>  $\times$  0.5.

For acute toxicity assay, all mice were sacrificed, and blood was collected via face piercing for serum chemistry studies. Major organs (including heart, liver, spleen, lungs, kidneys) were harvested for H&E staining and histological analysis.

For the rechallenge study, surviving BALB/c mice ( $n = 4$ ) after ONc-Mn-A-malF127 treatment were injected subcutaneously with  $1 \times 10^6$  CT26 cells (right flank) on day 60. Additional control mice ( $n = 4$ ) were implanted with same tumor cells for comparison, followed by tumor volume measurement up to 40 days.

**In Vivo Analysis for Immune Responses.** At indicated times, tumor draining lymph nodes (TDLNs), spleen, and tumor tissues were collected, cut into small pieces, and treated with collagenase type IV (1 mg mL<sup>-1</sup>) and DNase I (0.1 mg mL<sup>-1</sup>) under gentle shaking. Then TdLN, spleen, and tumor tissues were ground and filtered through a 40  $\mu\text{m}$  strainer to obtain single cell suspensions. To remove erythrocytes, erythrocyte lysate was added to the cell suspension for 5 min on ice. To quantify the maturation of the DCs, cells obtained from TDLNs and tumor tissues were stained with APC–anti-mouse CD11c antibody, FITC–anti-mouse CD40 antibody, and PerCP-Cy5.5–anti-mouse CD86 antibody and incubated on ice for 40 min. To assess immune infiltrate phenotyping, cells obtained from spleen and tumor tissues were treated on ice with PE–anti-mouse CD4<sup>+</sup>,

FITC–anti-mouse CD3<sup>+</sup>, PerCP/Cy5.5–anti-mouse CD45, PE–anti-human/mouse granzyme B recombinant and APC–anti-mouse CD8<sup>+</sup> antibodies for staining. To evaluate macrophage repolarization and NK cell activation in the tumor microenvironment, cells obtained from tumor tissues were stained with FITC–anti-mouse CD45, PerCP/Cy5.5–anti-mouse CD86, PE/Cy7–anti-mouse CD107a, APC–anti-mouse CD49b (pan-NK cells), FITC–anti-mouse CD3<sup>+</sup>, and PerCP/Cy5.5–anti-mouse CD45 antibodies on ice. Forty minutes after all cells were stained, cells were washed twice with PBS and used for flow cytometry analysis (Becton Dickinson FACS Aria III); the data were analyzed using FlowJo software. To test cytokine secretion, blood from mice was centrifuged to obtain serum for IFN $\beta$ , TNF $\alpha$ , and CXCL10 cytokine ELISA detection.

**Statistical Analysis.** Data are given as mean  $\pm$  standard deviation (SD). Flow cytometry results were analyzed with FlowJo v10. NIR fluorescence images were analyzed with Living Image 4.3 software. The statistical significance of tumor growth and survival rates was calculated via two-way ANOVA with Tukey's test and log-rank test, respectively. For multiple comparisons, one-way analysis of variance (ANOVA) with Tukey's post hoc test was used. The level of significance was defined as \* $p < 0.05$ , \*\* $p < 0.01$ , \*\*\* $p < 0.001$ , \*\*\*\* $p < 0.0001$ . All statistical analyses were performed using GraphPad Prism 8.0 software. All the data supporting the findings of this study are available within the article and its [Supporting Information](#) files and from the corresponding author upon reasonable request. A reporting summary for this article is available as a [Supporting Information](#) file.

## ASSOCIATED CONTENT

### Supporting Information

The Supporting Information is available free of charge at <https://pubs.acs.org/doi/10.1021/acsnano.2c06926>.

Description of synthesis of STING agonist ABZI derivative and of maleimide F127, <sup>1</sup>H and <sup>13</sup>C NMR, EA, and MS of compounds 2–8, mass spectrum of compound 8, <sup>1</sup>H NMR spectrum of maleimide-modified Pluronic F127, fluorescence spectra and UV–vis–NIR absorbance spectra of the different samples, representative flow cytometry plots of mature DCs, CD8<sup>+</sup> T cells, and CD4<sup>+</sup> T cells in spleens, tumor growth in survivors rechallenged with CT26 tumor cells on day 60, photothermal heating curves of ONc-Mn-A-malF127 nanoparticles and induced immunogenic cell death in vitro, IR thermal images, primary and distant tumor growth, toxicity analysis of different samples, hematoxylin and eosin analysis of major organs after systemic injections of different sample formulations, representative flow cytometry plots and quantification of mature DCs, CD8<sup>+</sup> T cells, and CD4<sup>+</sup> T cells in spleens and TDPAs by captured by ONc-Mn-A-malF127 ([PDF](#))

## AUTHOR INFORMATION

### Corresponding Author

Yumiao Zhang – School of Chemical Engineering and Technology, Key Laboratory of Systems Bioengineering (Ministry of Education), Frontiers Science Center for Synthetic Biology (Ministry of Education), Tianjin University, Tianjin 300350, P. R. China; [orcid.org/0000-0002-6166-0470](https://orcid.org/0000-0002-6166-0470); Email: [ymzhang88@tju.edu.cn](mailto:ymzhang88@tju.edu.cn)

### Authors

Jiexin Li – School of Chemical Engineering and Technology, Key Laboratory of Systems Bioengineering (Ministry of Education), Frontiers Science Center for Synthetic Biology

(Ministry of Education), Tianjin University, Tianjin 300350, P. R. China

He Ren – School of Chemical Engineering and Technology, Key Laboratory of Systems Bioengineering (Ministry of Education), Frontiers Science Center for Synthetic Biology (Ministry of Education), Tianjin University, Tianjin 300350, P. R. China

Qian Qiu – School of Chemical Engineering and Technology, Key Laboratory of Systems Bioengineering (Ministry of Education), Frontiers Science Center for Synthetic Biology (Ministry of Education), Tianjin University, Tianjin 300350, P. R. China

Xingyue Yang – School of Chemical Engineering and Technology, Key Laboratory of Systems Bioengineering (Ministry of Education), Frontiers Science Center for Synthetic Biology (Ministry of Education), Tianjin University, Tianjin 300350, P. R. China

Jingyu Zhang – School of Chemical Engineering and Technology, Key Laboratory of Systems Bioengineering (Ministry of Education), Frontiers Science Center for Synthetic Biology (Ministry of Education), Tianjin University, Tianjin 300350, P. R. China

Chen Zhang – School of Chemical Engineering and Technology, Key Laboratory of Systems Bioengineering (Ministry of Education), Frontiers Science Center for Synthetic Biology (Ministry of Education), Tianjin University, Tianjin 300350, P. R. China

Boyang Sun – School of Chemical Engineering and Technology, Key Laboratory of Systems Bioengineering (Ministry of Education), Frontiers Science Center for Synthetic Biology (Ministry of Education), Tianjin University, Tianjin 300350, P. R. China

Jonathan F. Lovell – Department of Biomedical Engineering, The State University of New York at Buffalo, Buffalo, New York 14260, United States; [orcid.org/0000-0002-9052-884X](https://orcid.org/0000-0002-9052-884X)

Complete contact information is available at: <https://pubs.acs.org/doi/10.1021/acsnano.2c06926>

### Author Contributions

Jiexin Li and Yumiao Zhang conceived the project. Jiexin Li carried out most experiments. He Ren and Qian Qiu assisted with material synthesis and animal experiments. Xingyue Yang, Chen Zhang, and Boyang Sun assisted with material synthesis and characterization. Jonathan Lovell assisted with manuscript editing. Jiexin Li and Yumiao Zhang performed data analysis and wrote the manuscript.

### Notes

The authors declare no competing financial interest.

## ACKNOWLEDGMENTS

This work was supported by National Natural Science Foundation of China (32071384), the National Key Research and Development Program (2021YFC2102300), Start-up Grant at Tianjin University, and One-thousand Young Talent Program of China.

## REFERENCES

- (1) McNutt, M. Cancer immunotherapy. *Science* **2013**, *342*, 1417–1417.
- (2) Huang, A. C.; Postow, M. A.; Orlowski, R. J.; Mick, R.; Bengsch, B.; Manne, S.; Xu, W.; Harmon, S.; Giles, J. R.; Wenz, B.; et al. T-cell

invigoration to tumour burden ratio associated with anti-PD-1 response. *Nature* **2017**, *545*, 60–65.

(3) Ribas, A.; Hamid, O.; Daud, A.; Hodi, F. S.; Wolchok, J. D.; Kefford, R.; Joshua, A. M.; Patnaik, A.; Hwu, W.-J.; Weber, J. S.; et al. Association of pembrolizumab with tumor response and survival among patients with advanced melanoma. *Jama* **2016**, *315*, 1600–1609.

(4) Syn, N. L.; Teng, M. W.; Mok, T. S.; Soo, R. A. De-novo and acquired resistance to immune checkpoint targeting. *Lancet Oncology* **2017**, *18*, e731–e741.

(5) McGranahan, N.; Rosenthal, R.; Hiley, C. T.; Rowan, A. J.; Watkins, T. B.; Wilson, G. A.; Birkbak, N. J.; Veeriah, S.; Van Loo, P.; Herrero, J.; et al. Allele-specific HLA loss and immune escape in lung cancer evolution. *Cell* **2017**, *171*, 1259–1271.

(6) Garrido, F.; Aptsiauri, N.; Doorduijn, E. M.; Garcia Lora, A. M.; van Hall, T. The urgent need to recover MHC class I in cancers for effective immunotherapy. *Current opinion in immunology* **2016**, *39*, 44–51.

(7) Nicolai, C. J.; Wolf, N.; Chang, I.-C.; Kim, G.; Marcus, A.; Ndubaku, C. O.; McWhirter, S. M.; Raulet, D. H. NK cells mediate clearance of CD8<sup>+</sup> T cell-resistant tumors in response to STING agonists. *Science immunology* **2020**, *5*, No. eaaz2738.

(8) Karlhofer, F. M.; Ribaud, R. K.; Yokoyama, W. M. MHC class I alloantigen specificity of Ly-49<sup>+</sup> IL-2-activated natural killer cells. *Nature* **1992**, *358*, 66–70.

(9) Kärre, K.; Ljunggren, H. G.; Piontek, G.; Kiessling, R. Selective rejection of H-2-deficient lymphoma variants suggests alternative immune defence strategy. *Nature* **1986**, *319*, 675–678.

(10) Yu, X.; Zhang, L.; Shen, J.; Zhai, Y.; Jiang, Q.; Yi, M.; Deng, X.; Ruan, Z.; Fang, R.; Chen, Z.; et al. The STING phase-separator suppresses innate immune signalling. *Nat. Cell Biol.* **2021**, *23*, 330–340.

(11) Sun, L.; Wu, J.; Du, F.; Chen, X.; Chen, Z. J. Cyclic GMP-AMP synthase is a cytosolic DNA sensor that activates the type I interferon pathway. *Science* **2013**, *339*, 786–791.

(12) Lorenzi, S.; Mattei, F.; Sisti, A.; Bracci, L.; Spadaro, F.; Sanchez, M.; Spada, M.; Belardelli, F.; Gabriele, L.; Schiavoni, G. Type I IFNs control antigen retention and survival of CD8 $\alpha$ <sup>+</sup> dendritic cells after uptake of tumor apoptotic cells leading to cross-priming. *J. Immunol.* **2011**, *186*, 5142–5150.

(13) Sivick, K. E.; Desbien, A. L.; Glickman, L. H.; Reiner, G. L.; Corrales, L.; Surh, N. H.; Hudson, T. E.; Vu, U. T.; Francica, B. J.; Banda, T.; et al. Magnitude of Therapeutic STING Activation Determines CD8<sup>+</sup> T Cell-Mediated Anti-tumor Immunity - ScienceDirect. *Cell Reports* **2019**, *29*, 785–789.

(14) Swann, J. B.; Hayakawa, Y.; Zerafa, N.; Sheehan, K.; Smyth, M. J.; et al. Type I IFN Contributes to NK Cell Homeostasis, Activation, and Antitumor Function. *J. Immunol.* **2007**, *178*, 7540–7549.

(15) Corrales, L.; Glickman, L. H.; McWhirter, S.; Kanne, D.; Sivick, K.; Katibah, G.; Woo, S. R.; Lemmens, E.; Banda, T.; Leong, J.; et al. Direct Activation of STING in the Tumor Microenvironment Leads to Potent and Systemic Tumor Regression and Immunity - ScienceDirect. *Cell Reports* **2015**, *11*, 1018–1030.

(16) Flood, B. A.; Higgs, E. F.; Li, S.; Luke, J. J.; Gajewski, T. F. STING pathway agonism as a cancer therapeutic. *Immunological Reviews* **2019**, *290*, 24.

(17) Kato, K.; Nishimasu, H.; Oikawa, D.; Hirano, S.; Hirano, H.; Kasuya, G.; Ishitani, R.; Tokunaga, F.; Nureki, O. Structural insights into cGAMP degradation by Ecto-nucleotide pyrophosphatase phosphodiesterase 1. *Nat. Commun.* **2018**, *9*, 4424.

(18) Chen, J.; Cao, Y.; Markelc, B.; Kaeppler, J.; Vermeer, J. A.; Muschel, R. J. Type I IFN protects cancer cells from CD8<sup>+</sup> T cell-mediated cytotoxicity after radiation. *J. Clin. Invest.* **2019**, *129*, 4224–4238.

(19) Lin, L. C.; Huang, C. Y.; Yao, B. Y.; Lin, J. C.; Agrawal, A.; Algaissi, A.; Peng, B. H.; Liu, Y. H.; Huang, P. H.; Juang, R. H.; Chang, Y. C.; Tseng, C. T.; Chen, H. W.; Hu, C. J. Viromimetic STING Agonist-Loaded Hollow Polymeric Nanoparticles for Safe and

Effective Vaccination against Middle East Respiratory Syndrome Coronavirus. *Adv. Funct. Mater.* **2019**, *29*, 1807616.

(20) Ramanjulu, J. M.; Pesiridis, G. S.; Yang, J.; Concha, N.; Singhaus, R.; Zhang, S. Y.; Tran, J. L.; Moore, P.; Lehmann, S.; Eberl, H. C.; Muelbauer, M.; Schneck, J. L.; Clemens, J.; Adam, M.; Mehlmann, J.; Romano, J.; Morales, A.; Kang, J.; Leister, L.; Graybill, T. L.; Charnley, A. K.; Ye, G.; Nevins, N.; Behnia, K.; Wolf, A. I.; Kasparcova, V.; Nurse, K.; Wang, L.; Puhl, A. C.; Li, Y.; Klein, M.; Hopson, C. B.; Guss, J.; Bantscheff, M.; Bergamini, G.; Reilly, M. A.; Lian, Y.; Duffy, K. J.; Adams, J.; Foley, K. P.; Gough, P. J.; Marquis, R. W.; Smothers, J.; Hoos, A.; Bertin, J. Design of amidobenzimidazole STING receptor agonists with systemic activity. *Nature* **2018**, *564*, 439–443.

(21) Humphries, F.; Shmuel-Galia, L.; Jiang, Z.; Wilson, R.; Landis, P.; Ng, S.-L.; Parsi, K. M.; Maehr, R.; Cruz, J.; Morales, A.; et al. A diamidobenzimidazole STING agonist protects against SARS-CoV-2 infection. *Science Immunology* **2021**, *6*, No. eabi9002.

(22) Horning, K. J.; Caito, S. W.; Tipps, K. G.; Bowman, A. B.; Aschner, M. Manganese is essential for neuronal health. *Annual review of nutrition* **2015**, *35*, 71.

(23) Kwakye, G. F.; Paoliello, M. M.; Mukhopadhyay, S.; Bowman, A. B.; Aschner, M. Manganese-induced parkinsonism and Parkinson's disease: shared and distinguishable features. *International journal of environmental research and public health* **2015**, *12*, 7519–7540.

(24) Waldron, K. J.; Rutherford, J. C.; Ford, D.; Robinson, N. J. Metalloproteins and metal sensing. *Nature* **2009**, *460*, 823–830.

(25) Lv, M.; Chen, M.; Zhang, R.; Zhang, W.; Wang, C.; Zhang, Y.; Wei, X.; Guan, Y.; Liu, J.; Feng, K.; Jing, M.; Wang, X.; Liu, Y.-C.; Mei, Q.; Han, W.; Jiang, Z. Manganese is critical for antitumor immune responses via cGAS-STING and improves the efficacy of clinical immunotherapy. *Cell Research* **2020**, *30*, 966–979.

(26) Sun, X.; Zhang, Y.; Li, J.; Park, K. S.; Han, K.; Zhou, X.; Xu, Y.; Nam, J.; Xu, J.; Shi, X.; Wei, L.; Lei, Y. L.; Moon, J. J. Amplifying STING activation by cyclic dinucleotide-manganese particles for local and systemic cancer metalloimmunotherapy. *Nat. Nanotechnol* **2021**, *16*, 1260–1270.

(27) Li, J.; Ren, H.; Zhang, Y. Metal-based nano-vaccines for cancer immunotherapy. *Coord. Chem. Rev.* **2022**, *455*, 214345.

(28) Zhao, Z.; Ma, Z.; Wang, B.; Guan, Y.; Su, X.-D.; Jiang, Z. Mn<sup>2+</sup> directly activates cGAS and structural analysis suggests Mn<sup>2+</sup> induces a noncanonical catalytic synthesis of 2' 3'-cGAMP. *Cell reports* **2020**, *32*, 108053.

(29) Gao, M.; Xie, Y. Q.; Lei, K.; Zhao, Y.; Kurum, A.; Van Herck, S.; Guo, Y.; Hu, X.; Tang, L. A Manganese Phosphate Nanocluster Activates the cGAS-STING Pathway for Enhanced Cancer Immunotherapy. *Advanced Therapeutics* **2021**, *4*, 2100065.

(30) Wang, Y.; Xie, Y.; Luo, J.; Guo, M.; Hu, X.; Chen, X.; Chen, Z.; Lu, X.; Mao, L.; Zhang, K.; Wei, L.; Ma, Y.; Wang, R.; Zhou, J.; He, C.; Zhang, Y.; Zhang, Y.; Chen, S.; Shen, L.; Chen, Y.; Qiu, N.; Liu, Y.; Cui, Y.; Liao, G.; Liu, Y.; Chen, C. Engineering a self-navigated MnARK nanovaccine for inducing potent protective immunity against novel coronavirus. *Nano Today* **2021**, *38*, 101139.

(31) Ma, Y.; Shurin, G. V.; Zhu, P.; Shurin, M. R. Dendritic Cells in the Cancer Microenvironment. *J. Cancer* **2013**, *4*, 36–44.

(32) Yan, J.; Wang, G.; Xie, L.; Tian, H.; Li, J.; Li, B.; Sang, W.; Li, W.; Zhang, Z.; Dai, Y. Engineering Radiosensitizer-Based Metal-Phenolic Networks Potentiate STING Pathway Activation for Advanced Radiotherapy. *Adv. Mater.* **2022**, *34*, No. e2105783.

(33) Deng, H.; Yang, W.; Zhou, Z.; Tian, R.; Lin, L.; Ma, Y.; Song, J.; Chen, X. Targeted scavenging of extracellular ROS relieves suppressive immunogenic cell death. *Nat. Commun.* **2020**, *11*, 4951.

(34) Galluzzi, L.; Buqué, A.; Kepp, O.; Zitvogel, L.; Kroemer, G. Immunogenic cell death in cancer and infectious disease. *Nature Reviews Immunology* **2017**, *17*, 97–111.

(35) Deng, H.; Zhou, Z.; Yang, W.; Lin, L. S.; Wang, S.; Niu, G.; Song, J.; Chen, X. Endoplasmic Reticulum Targeting to Amplify Immunogenic Cell Death for Cancer Immunotherapy. *Nano Lett.* **2020**, *20*, 1928–1933.

- (36) Min, Y.; Roche, K. C.; Tian, S.; Eblan, M. J.; McKinnon, K. P.; Caster, J. M.; Chai, S.; Herring, L. E.; Zhang, L.; Zhang, T.; DeSimone, J. M.; Tepper, J. E.; Vincent, B. G.; Serody, J. S.; Wang, A. Z. Antigen-capturing nanoparticles improve the abscopal effect and cancer immunotherapy. *Nat. Nanotechnol* **2017**, *12*, 877–882.
- (37) Fan, M.; Jia, L.; Pang, M.; Yang, X.; Yang, Y.; Kamel Elyazaty, S.; Liao, Y.; Wang, H.; Zhu, Y.; Wang, Q. Injectable Adhesive Hydrogel as Photothermal-Derived Antigen Reservoir for Enhanced Anti-Tumor Immunity. *Adv. Funct. Mater.* **2021**, *31*, 2010587.
- (38) Wang, M.; Song, J.; Zhou, F.; Hoover, A. R.; Murray, C.; Zhou, B.; Wang, L.; Qu, J.; Chen, W. R. NIR-Triggered Phototherapy and Immunotherapy via an Antigen-Capturing Nanoplatfor for Metastatic Cancer Treatment. *Adv. Sci. (Weinh)* **2019**, *6*, 1802157.
- (39) Zhang, R.; Wang, C.; Guan, Y.; Wei, X.; Sha, M.; Yi, M.; Jing, M.; Lv, M.; Guo, W.; Xu, J.; Wan, Y.; Jia, X. M.; Jiang, Z. Manganese salts function as potent adjuvants. *Cell Mol. Immunol* **2021**, *18*, 1222–1234.
- (40) Chen, Q.; Sun, L.; Chen, Z. J. Regulation and function of the cGAS-STING pathway of cytosolic DNA sensing. *Nat. Immunol* **2016**, *17*, 1142–9.
- (41) Kwon, J.; Bakhroum, S. F. The Cytosolic DNA-Sensing cGAS-STING Pathway in Cancer. *Cancer Discov* **2020**, *10*, 26–39.
- (42) Sivick, K. E.; Desbien, A. L.; Glickman, L. H.; Reiner, G. L.; Corrales, L.; Surh, N. H.; Hudson, T. E.; Vu, U. T.; Francica, B. J.; Banda, T.; et al. Magnitude of therapeutic STING activation determines CD8+ T cell-mediated anti-tumor immunity. *Cell Reports* **2019**, *29*, 785–789.
- (43) Kato, K.; Nishimasu, H.; Oikawa, D.; Hirano, S.; Hirano, H.; Kasuya, G.; Ishitani, R.; Tokunaga, F.; Nureki, O. Structural insights into cGAMP degradation by Ecto-nucleotide pyrophosphatase phosphodiesterase 1. *Nat. Commun.* **2018**, *9*, 4424.
- (44) Di Virgilio, F.; Sarti, A. C.; Falzoni, S.; De Marchi, E.; Adinolfi, E. Extracellular ATP and P2 purinergic signalling in the tumour microenvironment. *Nature Reviews Cancer* **2018**, *18*, 601–618.
- (45) Li, L.; Yin, Q.; Kuss, P.; Maliga, Z.; Millán, J. L.; Wu, H.; Mitchison, T. J. Hydrolysis of 2' 3'-cGAMP by ENPPI and design of nonhydrolyzable analogs. *Nat. Chem. Biol.* **2014**, *10*, 1043–1048.
- (46) Gajewski, T. F.; Higgs, E. F. Immunotherapy with a sting. *Science* **2020**, *369*, 921–922.
- (47) Liang, Y.; Hannan, R.; Fu, Y.-X. Type I IFN activating type I dendritic cells for antitumor immunity. *Clin. Cancer Res.* **2021**, *27*, 3818–3824.
- (48) Fuertes, M. B.; Woo, S.-R.; Burnett, B.; Fu, Y.-X.; Gajewski, T. F. Type I interferon response and innate immune sensing of cancer. *Trends in immunology* **2013**, *34*, 67–73.
- (49) Meric-Bernstam, F.; Sandhu, S. K.; Hamid, O.; Spreafico, A.; Kasper, S.; Dummer, R.; Shimizu, T.; Steeghs, N.; Lewis, N.; Talluto, C. C.; Dolan, S.; Bean, A.; Brown, R.; Trujillo, D.; Nair, N.; Luke, J. J. Phase Ib study of MIW815 (ADU-S100) in combination with spartalizumab (PDR001) in patients (pts) with advanced/metastatic solid tumors or lymphomas. *Journal of Clinical Oncology* **2019**, *37*, 2507–2507.
- (50) Spranger, S.; Dai, D.; Horton, B.; Gajewski, T. F. Tumor-residing Batf3 dendritic cells are required for effector T cell trafficking and adoptive T cell therapy. *Cancer cell* **2017**, *31*, 711–723.
- (51) Vivier, E.; Raulet, D. H.; Moretta, A.; Caligiuri, M. A.; Zitvogel, L.; Lanier, L. L.; Yokoyama, W. M.; Ugolini, S. Innate or adaptive immunity? The example of natural killer cells. *science* **2011**, *331*, 44–49.
- (52) Swann, J. B.; Hayakawa, Y.; Zerafa, N.; Sheehan, K. C.; Scott, B.; Schreiber, R. D.; Hertzog, P.; Smyth, M. J. Type I IFN contributes to NK cell homeostasis, activation, and antitumor function. *J. Immunol.* **2007**, *178*, 7540–7549.
- (53) Moses, A. S.; Taratula, O. R.; Lee, H.; Luo, F.; Grenz, T.; Korzun, T.; Lorenz, A. S.; Sabei, F. Y.; Bracha, S.; Alani, A. W. G.; Slayden, O. D.; Taratula, O. Nanoparticle-Based Platform for Activatable Fluorescence Imaging and Photothermal Ablation of Endometriosis. *Small* **2020**, *16*, No. e1906936.
- (54) Zhang, Y.; Jeon, M.; Rich, L. J.; Hong, H.; Geng, J.; Zhang, Y.; Shi, S.; Barnhart, T. E.; Alexandridis, P.; Huizinga, J. D.; Seshadri, M.; Cai, W.; Kim, C.; Lovell, J. F. Non-invasive multimodal functional imaging of the intestine with frozen micellar naphthalocyanines. *Nat. Nanotechnol.* **2014**, *9*, 631–638.
- (55) Zhang, Y.; Hong, H.; Sun, B.; Carter, K.; Qin, Y.; Wei, W.; Wang, D.; Jeon, M.; Geng, J.; Nickles, R. J.; Chen, G.; Prasad, P. N.; Kim, C.; Xia, J.; Cai, W.; Lovell, J. F. Surfactant-stripped naphthalocyanines for multimodal tumor theranostics with upconversion guidance cream. *Nanoscale* **2017**, *9*, 3391–3398.
- (56) Sistigu, A.; Yamazaki, T.; Vacchelli, E.; Chaba, K.; Enot, D. P.; Adam, J.; Vitale, I.; Goubar, A.; Baracco, E. E.; Remédios, C.; et al. Cancer cell–autonomous contribution of type I interferon signaling to the efficacy of chemotherapy. *Nature medicine* **2014**, *20*, 1301–1309.
- (57) Tian, H.; Wang, G.; Sang, W.; Xie, L.; Zhang, Z.; Li, W.; Yan, J.; Tian, Y.; Li, J.; Li, B.; Dai, Y. Manganese-phenolic nanoadjuvant combines sonodynamic therapy with cGAS-STING activation for enhanced cancer immunotherapy. *Nano Today* **2022**, *43*, 101405.
- (58) Chen, D. S.; Mellman, I. Oncology meets immunology: the cancer-immunity cycle. *immunity* **2013**, *39*, 1–10.
- (59) Jiang, Y.; Huang, J.; Xu, C.; Pu, K. Activatable polymer nanoagonist for second near-infrared photothermal immunotherapy of cancer. *Nat. Commun.* **2021**, *12*, 742.
- (60) Sanmamed, M. F.; Chen, L. A paradigm shift in cancer immunotherapy: from enhancement to normalization. *Cell* **2018**, *175*, 313–326.
- (61) Li, J.; Ren, H.; Sun, Y.; Liu, G.; Yang, X.; Qiu, Q.; Ding, Y.; Lovell, J. F.; Zhang, Y. Magnetic Metal Micelles for Enhanced Delivery of Self-Immolating CD8+ T-Cell Epitopes for Cancer Immunotherapy. *Chem. Mater.* **2021**, *33*, 9780–9794.
- (62) Luo, Z.; He, T.; Liu, P.; Yi, Z.; Zhu, S.; Liang, X.; Kang, E.; Gong, C.; Liu, X. Self-Adjuvanted Molecular Activator (SeaMac) Nanovaccines Promote Cancer Immunotherapy. *Adv. Healthcare Mater.* **2021**, *10*, 2002080.

## Recommended by ACS

### Stimuli-Responsive Polymeric Nanovaccines Toward Next-Generation Immunotherapy

Liuzhou Mao, Zibiao Li, et al.

MAY 19, 2023  
ACS NANO

READ 

### Liquid Metal Nanoplatfor Based Autologous Cancer Vaccines

Dawei Wang, Wei Rao, et al.

MAY 30, 2023  
ACS NANO

READ 

### Nanovaccines Fostering Tertiary Lymphoid Structure to Attack Mimicry Nasopharyngeal Carcinoma

Zhenfu Wen, Lixin Liu, et al.

APRIL 14, 2023  
ACS NANO

READ 

### Normalizing the Immune Macroenvironment via Debulking Surgery to Strengthen Tumor Nanovaccine Efficacy and Eliminate Metastasis

Nana Ma, Xiao Zhao, et al.

DECEMBER 19, 2022  
ACS NANO

READ 

Get More Suggestions >